2014

Nonlinear Optical Studies of Photoelastic Effect and Magneto-Plasmonics

Wei Zheng
College of William & Mary - Arts & Sciences

Nonlinear Optical Studies of Photoelastic Effect and Magneto-Plasmonics

Wei Zheng

Tianjin & Inner Mongolia, China

MS, College of William and Mary, 2009
MS, Shenzhen University, 2007
BS, Nankai University, 2002

A Dissertation presented to the Graduate Faculty
of the College of William and Mary in Candidacy for the Degree of
Doctor of Philosophy

Department of Applied Science

The College of William and Mary
May 2014

APPROVAL PAGE

This Dissertation is submitted in partial fulfillment of
the requirements for the degree of

Doctor of Philosophy

Wei Zheng

Approved by the Committee, April, 2014

Committee Chair
Professor Gunter Lüpke, Department of Applied Science
College of William and Mary

Professor Michael Kelley, Department of Applied Science
College of William and Mary

Assistant Professor Mumtaz Qazilbash, Department of Physics
College of William and Mary

(for Aubrey Hanbicki)
Dr. Aubrey Hanbicki
Naval Research Lab

ABSTRACT

Nonlinear optical (NLO) processes are optical phenomena involving a nonlinear response to an applied light field. Two kinds of nonlinearities are studied in this dissertation: magnetic-induced second-harmonic generation (MSHG) interacting with surface plasmon, called "nonlinear magneto-plasmonics" (NMP), and the nonlinear index induced by a strong pump beam in Titanium doped sapphire crystal, referred to as population-induced nonlinear index effect.

The fundamentals of the major effects involved are discussed, which include: surface plasmon and its field enhancement effect, MSHG technique and phenomenological calculations, the contrast ratio of magnetic switching, the calculation of lensing effects, population induced strain, and photoelastic effect. Furthermore, the experimental techniques and setup are presented. Two ultrafast laser systems and the design of a spatially and temporally homogenized chirped pulse amplifier are also elaborated, because these are the most important devices in the experiments.

In the study of population-induced nonlinear index effect, a fast measurement system is developed and one of the photoelastic constants of Ti:sapphire is obtained, which is useful to optimize Ti:sapphire lasers and amplifiers. In the study of NMP, the MSHG signal enhancement effect and the magnetic contrast tuning effect are discovered in a single crystal iron film. The two-jump switching process induced by the cubic magnetic anisotropy of the iron film opens the way for simultaneously investigating both longitudinal and transverse magnetization components regardless of the external magnetic field. This study has potential usage in quaternary magnetic storage systems because it enables the read-out of all four magnetization states from crystalline iron with high contrast ratio, and it is also of interest for bio-chemical sensor applications due to its very high surface sensitivity and simple structure.

TABLE OF CONTENTS

Acknowledgements		ii
Dedications		iii
List of Figures		iv
Chapter 1.	Introduction	2
Chapter 2.	Theoretical Considerations and Simulation	16
Chapter 3.	Experimental Section	36
Chapter 4.	Population-Induced Photoelastic Lensing Effect	62
Chapter 5.	Nonlinear Magneto Plasmonics	72
Chapter 6.	Conclusion	89
Bibliography		90

ACKNOWLEDGEMENTS

My first acknowledgement must go to my advisor, Professor Gunter Lüpke. I would never have been able to finish my dissertation without his support and guidance. I would like to express my deepest gratitude to him, for his excellent supervision, patience, and providing me with excellent research atmosphere and equipments. Countless things that I learned from him will benefit me in many ways throughout my career.

I would like to thank my doctoral dissertation committee members: Prof. Michael Kelley of Applied Science Department, Prof. Mumtaz Qazilbash of Physics Department and Dr. Aubrey Hanbicki of Naval Research Lab, for their comments and suggestions for this dissertation. Their academic support and input are greatly appreciated.

I would also like to thank my senior students in Prof. Gunter Lüpke's group: Dr. Shuyan Zhang, Dr. Haibin Zhao, Dr. Yichun Fan, as well as other students: Xin Ma, Fan Fang and Haowei Zhai for their help during my years in the College of William and Mary. I appreciate our collaborators Dr. Berry Jonker and Dr. Aubrey Hanbicki of Navel research lab for their work on sample growth, discussion and polishing of manuscripts.

I am indebted to my small family here and larger family back in China. Their support is always the sweetest. I own special thanks to my sister Dr. Yuan Zhao and brother-in-low Dr. Taiping Wang. Their encouragements brought me to this country for a higher degree and their support has always been with me during these years.

My acknowledgement must also go to Mr. Xin Zhao, who is my high school physics teacher and my favorite teacher ever. He guided me to the road of physics and ignited my dream of being a scientist.

This Ph.D. is dedicated to my parents.
For their endless love, support and encouragement

LIST OF FIGURES

1. Surface SHG is sensitive to the surface and interface 3
2. Surface plasmon 6
3. Surface plasma has more direct effect on nonlinear magneto-plasmonics over magneto-plasmonics 8
4. Lensing effect for a laser beam 11
5. Excited TiO_6 complex applies strain to the crystal structure in a Titanium doped sapphire crystal 13
6. Kretschmann-Raether configuration for nonlinear magneto plasmonics: 0 is the coupler made of the quartz, 1 is the single crystal iron film grown on MgO substrate, and 2 is air, the index matching oil is applied between 0 and 1 17
7. Simulated ATR curve and field enhancement for a 40 nm gold layer by Kretschmann-Raether configuration 19
8. Simulated ATR curve and field enhancement for a 10 nm iron layer by Kretschmann-Raether configuration 19
9. Longitudinal and transverse MSHG and the Cartesian coordinates 20
10. MSHG hysteresis loop (one jump) 24
11. MSHG hysteresis loop (two jump) 25
12. Temperature distribution of a Brewster cut Ti:Sapphire crystal pumped by a 20 W laser beam, simulated by FEA software COMSOL 30
13. The excited state of TiO_6 complex expands as an ellipsoid 32
14. Specs of the laser pulse in different stages of a typical CPA 39
15. Energy distribution of a single mode Gaussian beam 42

16. Fluence distribution along the light path in the Ti:sapphire crystal. Pumping from both sides (red) is more homogeneous than from single side (blue) 43

17. Split, reverse and recombine to spread the hot spots 44

18. Real beam profile before and after recombination 44

19. K values in various situations 45

20. Pump pulse duration with (red and green lines) and without (blue line) delay 47

21. Overall layout of the pump scheme 48

22. Picosecond laser system for surface plasmon excitation and second harmonic generation 50

23. Kretschmann-Raether configuration: 0 is the coupler made of the quartz, 1 is the metal film, and 2 is air 53

24. Experimental setup of nonlinear magneto plasmonics 54

25. Retroreflector 55

26. The arrangement of lasers in the study of photoelastic effect 56

27. Data gathering system for the very fast photoelastic effect 58

28. Comparison between geometrical optics approximation (diamond) and Gaussian beam propagation (circle) calculations 60

29. The oscilloscope catches every pulse from the seed beam 61

30. Time dependent measurement of the lensing effect (pump energy is 500 mJ), (a) original data and the fitted curve, (b) calculated focal length based on the fitted curve 63

31. Comparison between the focal length of the crystal measured by oscilloscope and measured directly using an iris and a power meter 64

32. Signal when the pump energy is 700 mJ and test beam is P-polarized (the red line is the relaxation curve if not saturated) 65

33. The pump beam profile taken by a CCD camera, QuantaRay PRO-290 66

34. Population density in the sagittal plan of the crystal when pump energy is 500 mJ 67

35. Radius dependent optical pass deformation (OPD) in sagittal plane and quadratic fit 70

36. Brewster cut Ti:Sapphire crystal with electric field vector perpendicular to the C-axis 71

37. Coordinate system of the experimental setup 75

38. (a) MSHG signal from sample I with large SP enhancement but no apparent magnetic contrast; (b) Sample II with large SP enhancement and huge magnetic contrast 76

39. MSHG signal strength under ATR configuration (SP enhanced) and under normal reflection configuration from sample II 77

40. (a) Contrast ratio of T-MSHG and T-MOKE under ATR condition; (b) and (c) hysteresis loops obtained when the incident angle is 45.6° for P-polarized light-in and P-polarized light-out configuration. T-MSHG has much larger contrast ratio than T-MOKE 78

41. *Simulated ATR and SHG for sample I (a) and II (b)* 80

42. (a) Field strength of Ex and Ez , (b) Simulated T-MSHG signal. Set 1: $\chi_{xxx}^{odd} / \chi_{xzz}^{odd}$ =1:100, Set 2: $\chi_{xxx}^{odd} / \chi_{xzz}^{odd}$ =100:1 82

43. (a) MSHG and (b) MOKE hysteresis loops under ATR configuration with different incident angle 83

44. Magnetic contrast of MSHG and MOKE under ATR 84

45. Phase difference and ratio of magnitude as a function of incident angle. (a) L-MSHG, (b) T-MSHG 87

Nonlinear Optical Studies of Photoelastic Effect and Magneto-Plasmonics

Chapter 1: Introduction

Nonlinear optical (NLO) processes or nonlinearities are optical phenomena involving a nonlinear response to a driving light field. Parametric nonlinearities and nonlinear index are two kinds of nonlinearities studied in this dissertation. Parametric nonlinearities[1-3] are optical responses based on high-order susceptibilities ($\chi^{(2)}, \chi^{(3)}...$) of a medium and include the effects such as second harmonic generation (SHG)[4], third harmonic generation (THG)[5], four-wave mixing, and optical parametric amplification and oscillation[6]. Nonlinear index is the change in refractive index in the presence of strong light intensity. For example, optical Kerr effect[7] gives rise to the self-focusing effect in lasers and self phase-modulation in optical fibers. In this dissertation, I studied two NLO effects, the magnetic-induced second harmonic generation (MSHG) interacting with surface plasmon, called "nonlinear magneto-plasmonics" (NMP), and the nonlinear index induced by a strong pump beam in Titanium doped sapphire crystal, which is called population-induced nonlinear index effect.

1.1 Parametric nonlinearities

In the electric-dipole approximation, the polarization **P**, which is induced by incident light in a medium, can be written as an expansion in powers of the optical electric field $\mathbf{E}(\omega)$[1-3]:

$$P(\omega, 2\omega, ...) = \chi^{(1)}E(\omega) + \chi^{(2)}E(\omega)E(\omega) + ... \qquad (1.1.1)$$

where $\chi^{(1)}$ is the linear optical susceptibility tensor and $\chi^{(2)}$ is the second-order nonlinear susceptibility tensor, which gives rise to SHG, taking into account that the 4th-rank susceptibility tensor representing the quadrupolar contributions is much smaller. SHG is only allowed in media without inversion symmetry because it is an even-order ($\chi^{(2)}$) NLO effect. Therefore, SHG can be generated only in noncentrosymmetric media or at surfaces or interfaces between centrosymmetric media where the inversion symmetry is broken.

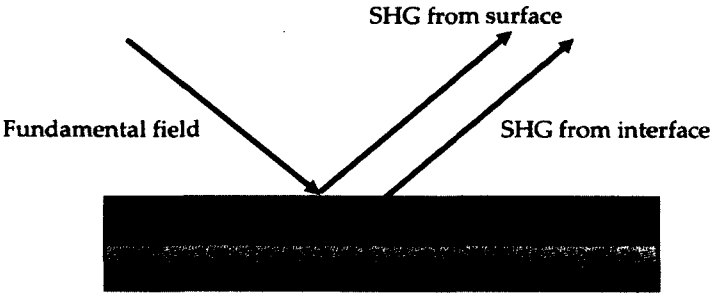

Figure 1.1.1 Surface SHG is sensitive to the surface and interface

For a centrosymmetric medium, the symmetry is broken in the first few atomic or molecular layers at the interface/surface and thus information about the interface/surface can be obtained by studying the properties of SHG signal, as shown in Fig. 1.1.1. Therefore, surface SHG provides a method to probe interface/surface in atomic or molecular systems. One can regard surface SHG as

a special case of SHG: 1) it is surface/interface sensitive, and 2) it is possible for some materials to not exhibit SHG in the bulk[1-3,8,9].

1.1.1 Magnetic induced second harmonic generation (MSHG)

For crystals with a magnetization M induced by spontaneous reasons or an external magnetic field, the second-order nonlinear optical polarization can be written as[10]:

$$P^{nl}(2\omega) = \chi^{cr} E(\omega)E(\omega) \pm \chi^{magn}(\pm M)E(\omega)E(\omega) \qquad (1.1.2)$$

where the first term on the right side describes the non-magnetic contribution or crystal contribution as elaborated in Eq. 1.1.1, while the second term describes MSHG, which exists only in the presence of a magnetization M. χ^{cr} and χ^{magn} are non-intermixing tensors for crystallographic contribution and magnetization, respectively[10].

MSHG was experimentally discovered in 1991 by Reif[11,12], and arose comprehensive research interests over the last decade because of the fast development and enormous applications of magnetic multi-layers and nano-structures. The availability of commercial mode-locked lasers suitable for harmonic generation also contributes to the study of MSHG. It is a powerful method for probing the interface/surface magnetization. MSHG has been demonstrated to be an extreme sensitivity technique to the slightest

modifications of the spin-polarized electronic structure of transition-metal interfaces and surfaces[13-26]. Since the magnetization leads to a polarization change of the second harmonic signal, MSHG effect is also called nonlinear magneto-optics (MO).

Besides the high sensitivity in the magnetization, MSHG technique has been demonstrated competent in the following applications: probing the magnetic properties of buried interfaces[27], distinguishing contributions from different interfaces[28], detecting antiferromagnetic ordering and imaging antiferromagnetic domains[29,30], and studying exchange-biased structures and their dynamics[31-36].

1.1.2 Surface plasmons and magneto-plasmonics

Surface plasmon (SP) is electromagnetic wave that propagates along metal-dielectric interfaces[37,38]. The charge fluctuations are localized in the direction normal to the surface within the Thomas-Fermi screening length of about 1 Å[37]. The field of SP is described by[37]

$$E = E_0 \exp[+i(k_x x \pm k_z z - \omega t)] \qquad (1.1.3)$$

where z is the direction normal to the surface , k_z is the imaginary wave vector, which causes the exponential decay of field E_z, x is the direction parallel to the surface, k_x is the real surface plasmon wave vector, indicating the propagation direction of the SP (Fig. 1.1.2), ω is the frequency of the wave, and t is the time.

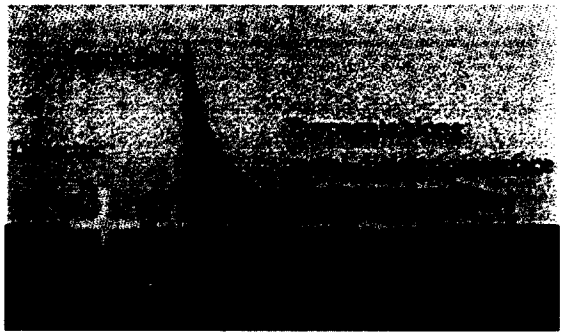

Figure 1.1.2 Surface plasmon

The electromagnetic field has its maximum at the surface and decays exponentially normal to the surface, which are the typical proprieties of a surface wave[39-41]. This explains the surface sensitivity and gives a prediction on possible application of sensors. The other most important feature of SP is a strong enhancement of the electromagnetic field at the metal-dielectric interface with the excitation of SP by light[37,42-44]. This field enhancement has many applications such as enhanced photoluminescence[45], enhancement of light scattered at Rayleigh waves[46], surface enhanced Raman scattering (SERS)[47], enhanced emission of light from tunnel junctions[48], bio-chemical sensors by enhanced magneto-optic Kerr effect (MOKE)[49-51], enhanced NLO processes like SHG[52] and THG[53], and four-wave mixing and MSHG[54].

Magneto-plasmonics (MP) describes hybrid systems where plasmonics and magnetic properties coexist, and has great potential for MO devices[55]. MP has generated much interest because of the potential applications in bio-chemical sensors[49-51] and the magnetic control/modulation of SPs[55,56]. As a traditional method to study MP effect, MOKE changes the polarization of incoming light when interacting with magnetic media. In general, it is typical to use a thick magnetic layer to obtain a large change of polarization because MOKE is a bulk effect. Historically, one dilemma for MP systems is that the noble metal layer supports high quality SP, but a very large magnetic field (several Tesla) is needed to achieve MO activity. On the other hand, the ferromagnetic (FM) layer exhibits large MO activity, which makes it possible to make real MO devices. However, the huge losses in the FM layer causes an over damping of plasmon resonance, and thus impairs the strength of SP. The prevailing configuration, noble metal/FM/noble metal heterostructures[49-51,56-59], combines the strength of good quality SP and large MO effect, but makes the structure complex and separates the source of SP and magnetization which compromises the coupling between them.

1.1.3 Nonlinear Magneto Plasmonics

In this dissertation, I use a nonlinear optical technique, MSHG, to study MP, called Nonlinear Magneto-Plasmonic (NMP) which refers to the nonlinear optical

response from MP system. As a surface sensitive MO effect, MSHG contains nonzero magnetic components of the second-order nonlinear susceptibility tensor which makes MSHG extremely sensitive to subtle modifications of the spin-polarized electronic structure of transition metal surfaces[13], the same region where SP is present. Many advantages are expected from NMP: 1) the field enhancement effect of SP makes the MSHG signal stronger, which is favorable for magnetic materials with smaller susceptibilities and lower damage threshold; 2) the overlap in geometry removes the need for complex hetero-structures, which is favorable for device development; 3) the direct contact of SP as a surface wave and MSHG source might bring some novel effects; 4) the combination of the two surface sensitive effects, SP and MSHG, makes it of interest for bio-chemical sensors (Fig. 1.1.3).

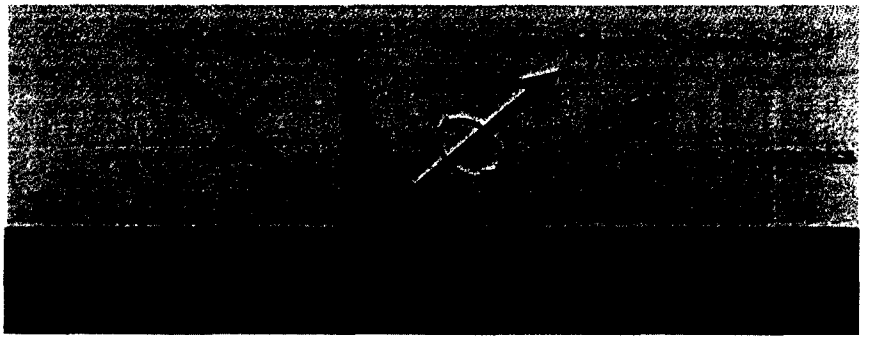

Figure 1.1.3 Surface plasma has more direct effect on nonlinear magneto-plasmonics over magneto-plasmonics

1.2 Nonlinear refractive index

The development of mode-locked ultrafast lasers plays a crucial role in the

research of nonlinear optics. The mode-locked technique is based on optical Kerr effect[60,61], which is a third-order ($\chi^{(3)}$) nonlinear optical effect and can be expressed as[7]

$$n = n_0 + \frac{3\chi^{(3)}}{8n_0}|E_\omega|^2 = n_0 + n_2 I, \qquad (1.2.1)$$

where I is the intensity of the light. Besides $\chi^{(3)}$, there are also other mechanisms that can contribute to the change of index n_2. For example, Pockels effect, which was discovered by Friedrich Carl Alwin Pockels in 1893, produces birefringence in an optical noncentrosymmetric medium induced by a constant or varying electric field[62]. Another example is the photoelastic effect, which was first described by David Brewster in early 19th century, which makes photoelastic materials exhibit birefringence upon the application of stresses[63,64] . Temperature can also change the index, since for most optical materials the refractive index is a function of temperature[65-67]. If this change is uneven, a beam going through the material will have a wave front deformation. If the change of index displays a radially gradual pattern, the beam will be focused/defocused, which is called lensing effect.

1.2.1 Lensing effect in lasers

The lensing effect in lasers and their applications are based on the property that a medium (normally, a solid state medium) becomes a lens that focuses the laser beams (Fig. 1.2.1). Lensing effects are very pronounced in modern high

average/peak power systems, especially for the solid state laser medium[68]. They change the resonance conditions of the laser cavity as well as the overall light path largely, and a focused beam might even damage the optics within or outside of the cavity. Therefore, the design of high power lasers and amplifiers needs to put the lensing effects into consideration[69-71]. So far, three major sources are accountable for the lensing effects: 1) Kerr lens effect, 2) Thermal-related effects, and 3) Population-related effects in the laser medium. All these lensing effects are a consequence of the change of refractive index, which leads to a gradual phase difference between the beam axis and edge[68]. This is similar to the function of a lens: the wavefronts are deformed, and as a result, the beam is focused. Kerr lens effect is induced by the beam itself, and it is strong for a focused beam with a short pulse-width and a large intensity. The thermal lensing effects exist in all solid state laser media and have been regarded as the dominant lensing effect for solid state lasers for a long time. The thermal lensing effects for Nd:YAG lasers were firstly published by Koechner in 1970[72]. After that, thermal lensing effects for other laser media, varieties of pumping methods and laser cavities were studied[73-79]. As a consequence, thermo-optic properties (refractive index as a function of temperature) of varieties of laser media were measured[79,80]. In most cases, the thermal effect is considered and measured as an average effect.

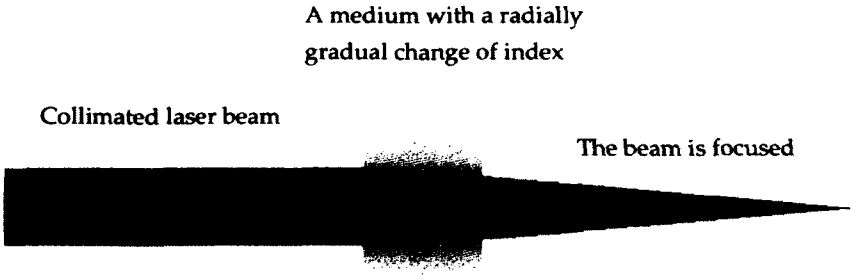

Figure 1.2.1 Lensing effect for a laser beam

Like other solid state lasers, the lensing effect needs to be considered seriously in a Ti:Sapphire chirped-pulse-amplifier (CPA) system. The lensing effect is harmful to the amplifier in the following major aspects[68,81-83]: 1) it restricts the amplification rate by decreasing the mode volume of the seed beam; 2) it introduces optical aberration in the system, which makes the seed beam profile worse; and 3) it may even damage the crystal by focusing the amplified seed beam. Taking a multi-pass amplifier system for instance, the Ti:sapphire crystal has saturated flux of 0.9 J/cm^2 and damage threshold of 5 J/ cm^2 [84-56], if the seed beam diameter is decreased by a factor of 2 due to lensing effect, the max amplification rate will be decreased at least 4 times; if the beam diameter is decreased to 2 mm, the pulse energy has to be limited to 100 mJ to prevent damage of the crystal. Furthermore, for an unfocused seed beam in a multi-pass amplifier, the Kerr lensing effect is very tiny. However, if the seed beam is focused, the Kerr lens effect will become pronounced when the seed beam passes the medium again. This makes the case even worse and is definitely not desired.

One should note that the lensing effect and the change of index are interactive effects. Given the change of index, the focal length of lensing effect can be calculated. Conversely, if the focal length of lensing effect is known, the change of index and thus the nonlinear refractive index coefficient can be determined.

1.2.2 Fast lensing effect induced by upper level population in Ti:Sapphire crystal

In the study of a CPA based on Ti:Sapphire crystal, besides the well-studied thermal-induced lensing effects, I am mainly interested in another kind of lensing effect which happens very fast (several microseconds) and can not be caught by the traditional measurement. This effect is induced by the nonlinear index which is caused by upper level population. Wall et al. firstly described this effect in 1989[87]. Eilers et al. performed fast measurement of the phase shift in Ti:sapphire crystal by beam-deflection spectroscopy and discussed thermal and nonthermal effects[88]. Planchon et al. performed time-resolved measurement in a nitrogen-cooled Ti:sapphire crystal by two-dimensional (2D) spectral interferometry[89]. The method to directly measure the focal length of this lensing effect has not been developed yet because it is pronounced only under strong pumping condition. Furthermore, the elasto-optical coefficients for Ti:sapphire crystal, which are important to calculate the lensing effect, are still missing. It is

urgent to realize such measurement and determine the coefficients for the design of high energy CPA.

The mechanism for this very fast lensing effect is[87]: 1) upper level population changes the micro and thus macro volume of the medium; 2) this volume change induces strain to the crystal structure (Fig. 1.2.2); 3) strain induces change of refractive index; and 4) change of index induces the lensing effect. All the involved effects will be elaborated in the following chapters and I will elaborate on how such effects work in specific cases.

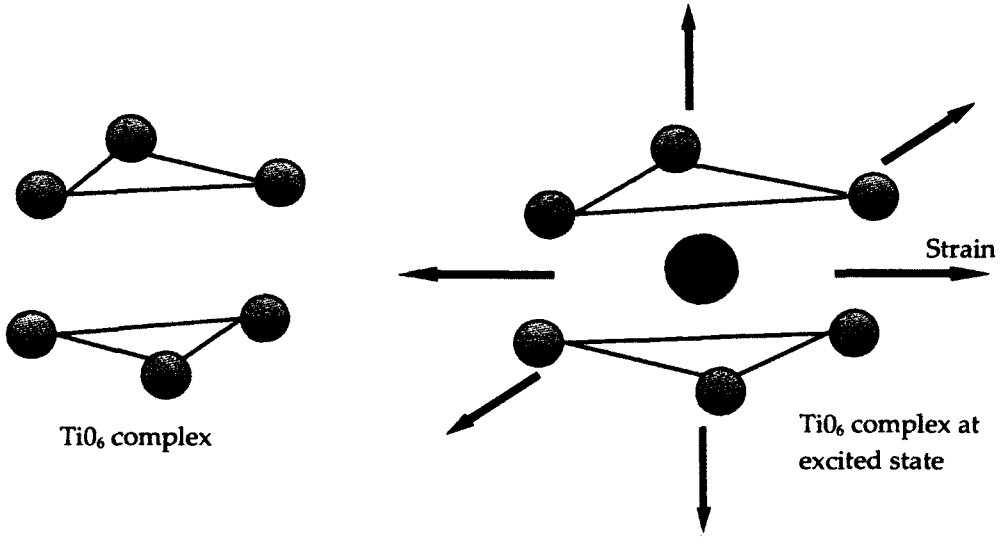

Figure 1.2.2 Excited TiO_6 complex applies strain to the crystal structure in a Titanium doped sapphire crystal

1.3 Outline

In chapter 2, the fundamentals of the major effects studied in this dissertation are discussed. Ch.2.1 is concerned with the field enhancement effect of SP. Ch.2.2 introduces tensors and calculations for MSHG. Ch.2.3 presents the contrast ratio of MSHG signal. The contrast ratio of two-jump system is derived for the first time here also. Ch.2.4 provides the calculation of lensing effects. Ch.2.5 focuses on population induced strain. Ch.2.6 treats the photoelastic effect and their tensors.

In chapter 3, the experimental setup and methods are elaborated. The ultra-fast laser system and the design of a spatially and temporally homogenized CPA are discussed in Ch.3.1. In Ch.3.2, the setup for NMP is presented, including the arrangement of laser systems (Ch.3.2.1), methods to excite the SP (Ch.3.2.2), and the data gathering system (Ch.3.2.3). In Ch.3.3, the unique experimental setup for detecting the fast population lensing effect directly is presented.

In chapter 4, the data of population lensing effect obtained by the fast measurement is analyzed (Ch.4.1). Then the optoelastic tensor of Ti:sapphire crystal is calculated, which filled the gap in this area (Ch.4.2).

In chapter 5, NMP is studied and results are presented, including the enhancement effect of both signal strength and magnetic contrast of transverse MSHG by SP (Ch.5.1), and the tuning effect of the contrast ratios of the MSHG hysteresis loop and the origin of such effect (Ch.5.2).

In Chapter 6, the work on nonlinear optical processes is summarized and the important findings and possible applications of this study are highlighted.

Chapter 2: Theoretical Considerations and Simulation

In this chapter, I present the theoretical description and related simulation of the fundamentals of the major effects studied in this dissertation. They include (1) the field enhancement effect of SP, (2) the tensors and calculations for MSHG, (3) the contrast ratios of MSHG signal for one-jump and two-jump systems, (4) the calculation of lensing effects, (5) the upper level population induced strain, and (6) the photoelastic effect and their tensors.

2.1 Field enhancement effect of SP under ATR configuration

Under Kretschmann-Raether configuration[37,90,91] (Fig. 2.1.1), the reflection as a function of the incident angle (also called ATR curve) for p-polarized light can be calculated by Fresnel's Equation as[37]

$$R = \left|\frac{E_r^p}{E_0^p}\right| = \left|\frac{r_{01}^p + r_{12}^p \exp(2ik_{z1}d)}{1 + r_{01}^p r_{12}^p \exp(2ik_{z1}d)}\right|^2, \qquad (2.1.1)$$

where E_0 is the incoming and E_r is the reflected field. For the three-layer system (Fig. 3.2.2), medium 0 is the coupler made of quartz or glass; medium 1 is the metal film of thickness d, medium 2 is dielectric, which is air in this case, p means p-polarized, and r_{ik}^p are the amplitude coefficients[37]:

$$r_{ik}^p = \left(\frac{k_{zi}}{\varepsilon_i} - \frac{k_{zk}}{\varepsilon_k}\right) \Big/ \left(\frac{k_{zi}}{\varepsilon_i} + \frac{k_{zk}}{\varepsilon_k}\right), \qquad (2.1.2)$$

where

$$k_{zi} = \left[\varepsilon_i \left(\frac{\omega}{c} \right)^2 - k_x^2 \right]^{1/2}, \qquad (2.1.3)$$

where ω is the frequency of light and c is the light speed in vacuum. The intensity of the electromagnetic field at the surface increases as the reflectivity R decreases. If medium 1 is a noble metal, e.g. Au, Ag, the reflectivity minimum represents maximum field or maximum field enhancement, which means a strong reduction of the reflected light corresponding to a complete transformation into SP.

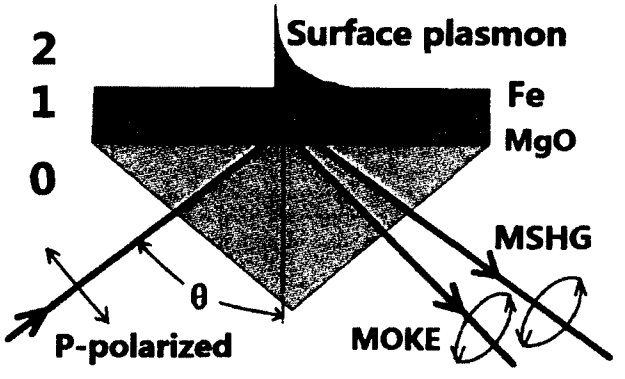

Figure 2.1.1 Kretschmann-Raether configuration for nonlinear magneto plasmonics: 0 is the coupler made of the quartz, 1 is the single crystal iron film grown on MgO substrate, and 2 is air, the index matching oil is applied between 0 and 1

The value of the field enhancement is given by the ratio of the field intensity on the metal surface (the metal/air interface) divided by the incoming field intensity in the prism (coupler/metal interface)[37]

$$En = \left| t_{012}^{p} \right|^2 = \frac{t_{01}^{p} t_{12}^{p} \exp(ik_{z1}d)}{1 + r_{01} r_{12} \exp(2ik_{z1}d_1)}, \qquad (2.1.4)$$

where $t_{ik}^{p} = 1 - r_{ik}^{p}$ are the corresponding coefficient of transmission in each boundary for p-polarized light, and $\left| t_{012}^{p} \right|$ represents Fresnel's transmission coefficient for the whole system. The maximum enhancement of the electric field intensity can be obtained by[37]

$$En_{\max} = \frac{\varepsilon_2}{\varepsilon_0} \left(\frac{|E(2/1)|^2}{|E_0(0/1)|^2} \right)_{\max} = \frac{\varepsilon_2}{\varepsilon_2} T_{\max}^{el} = \frac{1}{\varepsilon_0} \cdot \frac{2|\varepsilon_1|^2}{\varepsilon_1''} \cdot \frac{\sqrt{|\varepsilon_1|(\varepsilon_0 - 1) - \varepsilon_0}}{1 + |\varepsilon_1|}, \qquad (2.1.5)$$

where $T_{\max}^{el}$ can be understood as the maximum Fresnel's transmission coefficient for the system, and ε_1' and ε_1'' are the real and imaginary part of the permittivity of the metal, respectively.

Based on Equations 2.1.1 to 2.1.4, the ATR curve and the field enhancement can be calculated. Figure 2.1.2 is for a 40 nm gold layer and Figure 2.1.3 is for a 10 nm iron layer. The ATR curve for iron is broadened due to the strong damping effect. The reflection coefficient (Eq. 2.1.1) has Lorentzian line shape, and can be expressed as[37]

$$R = 1 - \frac{4\Gamma_i \Gamma_{rad}}{\left[(k_x - k_x^0)^2 + (\Gamma_i + \Gamma_{rad})^2 \right]}, \qquad (2.1.6)$$

where Γ_i is the damping due to resistive heating, Γ_{rad} is the damping due to re-radiation into the prism, and k_x^0 is the wave vector with maximum coupling (resonance wave vector).

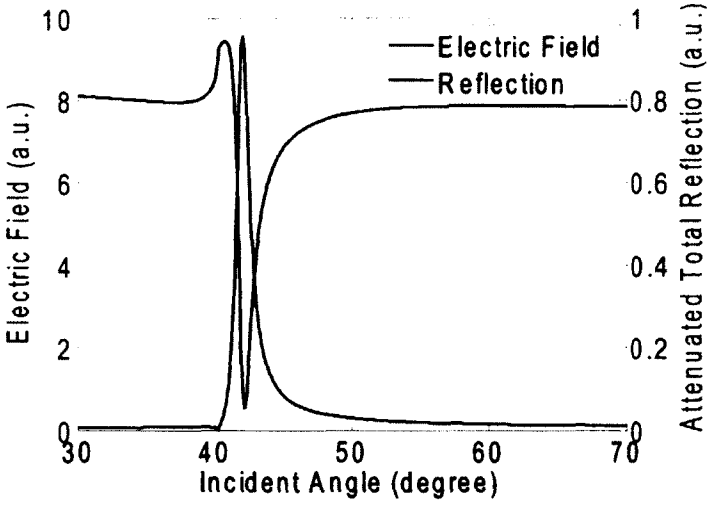

Figure 2.1.2 Simulated ATR curve and field enhancement for a 40 nm gold layer by Kretschmann-Raether configuration

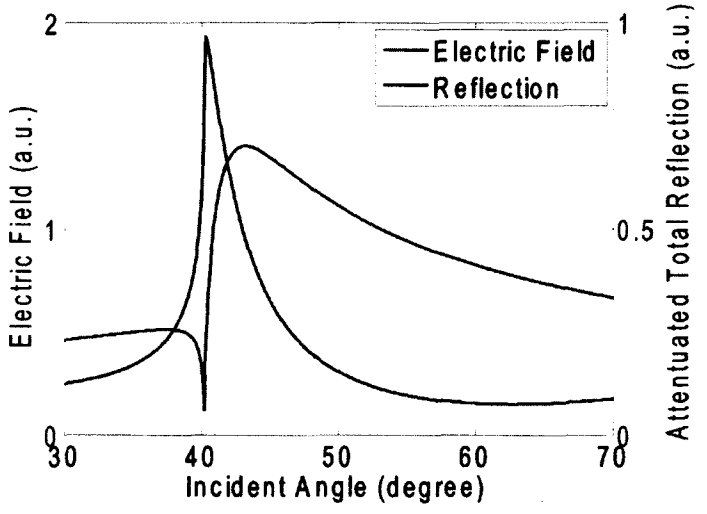

Figure 2.1.3 Simulated ATR curve and field enhancement for a 10 nm iron layer by Kretschmann-Raether configuration

The field enhancement of SP for a noble metal layer, e.g. gold, silver, with an optimized thickness is very strong, while it is also considerable for metal with strong damping like iron.

2.2 Magnetic induced second harmonic generation

In a Cartesian coordinate system, second harmonic polarization can be defined as

$$P_i(2\omega) = \chi^{cr}_{ijk} E_j(\omega) E_k(\omega), \qquad (2.2.1)$$

where i, j, and k are the Cartesian coordinates and χ^{cr} is the susceptibility tensor arising from the crystal structure. Taking into account the interchangeable electric fields and the broken inversion symmetry along the direction normal to the sample surface (z-direction), the tensors can be simplified and Equation 2.2.1 can be written as[1,5]

$$\begin{pmatrix} P_x \\ P_y \\ P_z \end{pmatrix} = \begin{pmatrix} 0 & 0 & 0 & 0 & \chi_{xzx} & 0 \\ 0 & 0 & 0 & \chi_{yzy} & 0 & 0 \\ \chi_{zxx} & \chi_{zyy} & \chi_{zzz} & 0 & 0 & 0 \end{pmatrix} \begin{pmatrix} E_x^2 \\ E_y^2 \\ E_z^2 \\ 2E_y^2 E_z^2 \\ 2E_z^2 E_x^2 \\ 2E_x^2 E_y^2 \end{pmatrix}. \qquad (2.2.2)$$

Figure 2.2.1 Longitudinal and transverse MSHG and the Cartesian coordinates

For MSHG, the direction of magnetization is also taken into consideration. As a result, the longitudinal (L-), transverse (T-), and polar MSHG are classified according to the direction of magnetization component with respect to the incident plane[10]. As shown in Figure 2.2.1, L- and T-MSHG are parallel to x- and y-axis, respectively. Here only L- and T-MSHG are discussed as the magnetization of a thin iron film studied in this dissertation is always in the sample plane (x-y plane). With proper simplification by symmetry, the nonlinear susceptibility tensors for L- and T-MSHG are derived as [10,92,93]

$$\chi_{ijk}^{(L)} = \begin{pmatrix} 0 & 0 & 0 & 0 & \chi_{xzx}^{even} & \chi_{xyx}^{odd} \\ \chi_{yxx}^{odd} & \chi_{yyy}^{odd} & \chi_{yzz}^{odd} & \chi_{yzy}^{even} & 0 & 0 \\ \chi_{zxx}^{even} & \chi_{zyy}^{even} & \chi_{zzz}^{even} & \chi_{zyz}^{even} & 0 & 0 \end{pmatrix} \qquad (2.2.3)$$

$$\text{and } \chi_{ijk}^{(T)} = \begin{pmatrix} \chi_{xxx}^{odd} & \chi_{xyy}^{odd} & \chi_{xzz}^{odd} & 0 & \chi_{xzx}^{even} & 0 \\ 0 & 0 & 0 & \chi_{yzy}^{even} & 0 & \chi_{yxy}^{odd} \\ \chi_{zxx}^{even} & \chi_{zyy}^{even} & \chi_{zzz}^{even} & 0 & \chi_{zxz}^{odd} & 0 \end{pmatrix}, \qquad (2.2.4)$$

where odd terms change signs with magnetization reversal and determine the switching process, while the even terms are not sensitive to magnetization and are considered as crystal contribution. Knowing the polarization of the incident beam, the second-order nonlinear optical polarization can be calculated by the tensors. For example, with an S-polarized incident beam (contains only E_y), the polarizations for L- and T- MSHG can be calculated as

$$\begin{pmatrix} P_x \\ P_y \\ P_z \end{pmatrix}^{(L)} = \chi_{ijk}^{(L)} \begin{pmatrix} 0 \\ E_y^2 \\ 0 \\ 0 \\ 0 \\ 0 \end{pmatrix} = \begin{pmatrix} 0 \\ \chi_{yyy}^{odd} E_y^2 \\ \chi_{yyy}^{even} E_y^2 \end{pmatrix} \tag{2.2.5}$$

$$\text{and} \quad \begin{pmatrix} P_x \\ P_y \\ P_z \end{pmatrix}^{(T)} = \chi_{ijk}^{(T)} \begin{pmatrix} 0 \\ E_y^2 \\ 0 \\ 0 \\ 0 \\ 0 \end{pmatrix} = \begin{pmatrix} \chi_{xyy}^{odd} E_y^2 \\ 0 \\ \chi_{yyy}^{even} E_y^2 \end{pmatrix}. \tag{2.2.6}$$

This means if an S-polarized analyzer is used, the detector only responses to $\chi_{yyy}^{odd} E_y^2$, if a P-polarized analyzer is used, the detector responses to $\chi_{yyy}^{even} E_y^2$ and $\chi_{xyy}^{odd} E_y^2$ because both x and z components contribute to E_p of the second-harmonic beam. In the same way, the polarization for L- and T- MSHG with a P-polarized fundamental field can be calculated as

$$\begin{pmatrix} P_x \\ P_y \\ P_z \end{pmatrix}^{(L)} = \chi_{ijk}^{(L)} \begin{pmatrix} E_x^2 \\ 0 \\ E_z^2 \\ 0 \\ 2E_z E_x \\ 0 \end{pmatrix} = \begin{pmatrix} \chi_{xzx}^{even} \cdot 2E_z E_x \\ \chi_{yxx}^{odd} \cdot E_x^2 + \chi_{yzz}^{odd} \cdot E_z^2 \\ \chi_{zxx}^{even} \cdot E_x^2 + \chi_{zzz}^{even} \cdot E_z^2 \end{pmatrix} \tag{2.2.7}$$

$$\text{and} \quad \begin{pmatrix} P_x \\ P_y \\ P_z \end{pmatrix}^{(T)} = \chi_{ijk}^{(T)} \begin{pmatrix} E_x^2 \\ 0 \\ E_z^2 \\ 0 \\ 2E_x E_z \\ 0 \end{pmatrix} = \begin{pmatrix} \chi_{xxx}^{odd} \cdot E_x^2 + \chi_{xzz}^{odd} \cdot E_z^2 + \chi_{xzx}^{even} \cdot 2E_z E_x \\ 0 \\ \chi_{zxx}^{even} \cdot E_x^2 + \chi_{zzz}^{even} \cdot E_z^2 + \chi_{zxz}^{odd} \cdot 2E_z E_x \end{pmatrix}. \tag{2.2.8}$$

2.3 Contrast ratio of MSHG

A very important concept for magneto-optical methods, i.e. MOKE and MSHG, is the contrast ratio or magnetic anisotropy of the hysteresis loop. It is defined by[10,93,94]

$$C = \frac{I(+M) - I(-M)}{I(+M) + I(-M)}, \tag{2.3.1}$$

where $I(+M)$ and $I(-M)$ are the MOKE/MSHG signal strength at two different magnetizations (Fig. 2.3.1). As both magnetic and non-magnetic crystal contributions are complex quantities, the MSHG signal can be written as

$$I^{2\omega} = \left|\chi_{eff}^{even}\right|^2 + \left|\chi_{eff}^{odd}\right|^2 \pm 2\left|\chi_{eff}^{even}\right|\left|\chi_{eff}^{odd}\right|\cos\Delta\Phi, \tag{2.3.2}$$

where $\Delta\Phi$ is the phase difference between the two contributions. χ_{eff} (even) and χ_{eff} (odd) are complex quantities including the involved nonlinear susceptibility tensors and the corresponding fields. As a result, the contrast ratio (Eq. 2.3.1) can be expressed as[10,95,96]

$$C = \frac{2\left|\chi_{eff}^{odd}\right| / \left|\chi_{eff}^{even}\right|}{1 + \left|\chi_{eff}^{odd} / \chi_{eff}^{even}\right|^2}\cos\Delta\Phi. \tag{2.3.3}$$

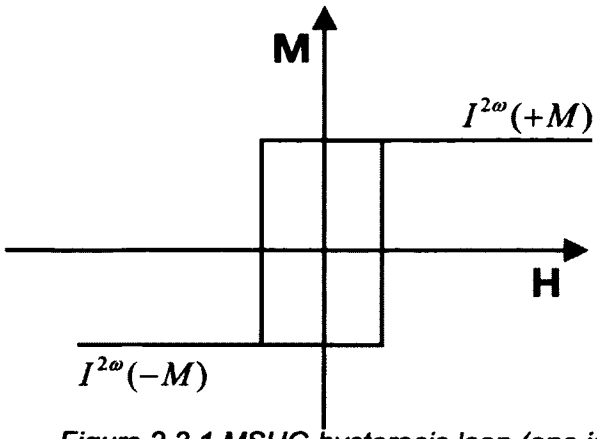

Figure 2.3.1 MSHG hysteresis loop (one jump)

The contrast ratio above is for the simplest case where there is only one jump in the hysteresis loop. However, materials with cubic magnetic anisotropy[93,97-99] (e.g., crystalline iron thin film) display two-jump switching in the hysteresis loop. Such case is systematically studied here and formulas are developed to determine the contrast ratio for a two-jump switch system.

Suppose the incident plane and the external magnetic field are parallel to the iron hard axis [-110] (Fig. 2.3.2). The L-component corresponds to the magnetization (M) component parallel to the plane-of-incidence, i.e., along the axis [-110], while the T-component is perpendicular[10], i.e., along the axis [110]. The magnetization of a thin Fe film is always in the sample plane if the external magnetic field (H) is applied parallel to the surface. The cubic magnetic anisotropy of single-crystal iron leads to two easy axes ([100] and [010]) and two hard axes ([110] and [-110]), and the magnetization tends to align along the easy axes (Fig. 2.3.2). Beginning

from an initial state M_I along [100], with increasing magnetic field along [-110], the magnetization overcomes the hard axis [110], which causes a change in the longitudinal magnetic component (M_I to M_{II}). As H increases further, the magnetization overcomes another hard axis [-110], which causes a change in the transverse magnetic component (M_{II} to M_{III}). The jumps from M_{II} to M_{III} and M_{IV} to M_I are possible because the external magnetic field can never be perfectly parallel to hard axis [-110], and a slight mis-orientation can cause such jumps. In the MSHG and MOKE hysteresis loops, each magnetization state corresponds to different signal intensity, I(M). The L-jump occurs at low coercivity while the T-jump happens at higher coercivity, as H is applied along the longitudinal direction and only a small field is needed to switch the L-component. From the two-jump hysteresis loops the L- and T- components can be separated clearly and studied simultaneously.

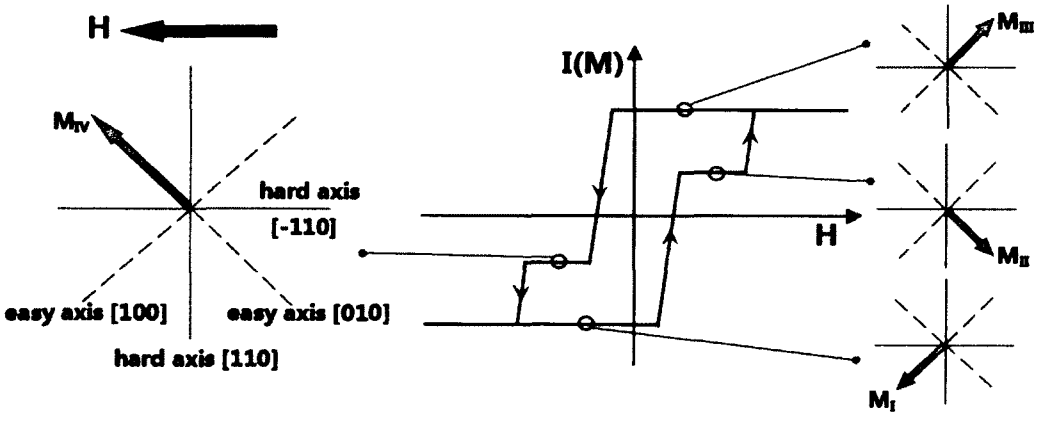

Figure 2.3.2 MSHG hysteresis loop (two jump)

In the same way as Eq.2.3.1, the T- and L- magnetic contrasts for two-jump loop are defined as:

$$C_T = \frac{(I(M_{III}) - I(M_{II})) + (I(M_{IV}) - I(M_I))}{I(M_I) + I(M_{II}) + I(M_{III}) + I(M_{IV})} \quad \text{and}$$

$$C_L = \frac{(I(M_{III}) - I(M_{IV})) + (I(M_{II}) - I(M_I))}{I(M_I) + I(M_{II}) + I(M_{III}) + I(M_{IV})}, \qquad (2.3.4)$$

where M_I, M_{II}, M_{III} and M_{IV} are depicted in Fig. 2.3.2. Next, expressions for the MSHG intensities $I^{2\omega}(M_i)$, $i= I,..,IV$ are derived. The total MSHG response (polarization) from a magnetic material can be simplified to

$$P(2\omega) = p^{even} \pm p_T^{odd} \pm p_L^{odd}, \qquad (2.3.5)$$

where p^{even} is the second-order polarization from the crystal, or the non-magnetic contribution, p_L^{odd} and p_T^{odd} are the magnetization-induced polarizations for L- and T- magnetization components, respectively, which change signs as magnetization reverses. Since these polarization contributions are complex quantities, involving fundamental fields, corresponding effective susceptibility tensors and polarization angles, the total (MSHG) signal is thus given by

$$\begin{aligned} I^{2\omega}(M_i) = &(p^{even})^2 + (p_T^{odd})^2 + (p_L^{odd})^2 \\ &\pm 2 \cdot p^{even} \cdot p_T^{odd} \cdot \cos\varphi_T \pm 2 \cdot p^{even} \cdot p_L^{odd} \cdot \cos\varphi_L \pm 2 \cdot p_L^{odd} \cdot p_T^{odd} \cdot \cos\varphi \end{aligned} \qquad (2.3.6)$$

Here ϕ_T is the phase difference between p^{even} and p_T^{odd}, ϕ_L is the phase difference between p^{even} and p_L^{odd}, and ϕ is the phase difference between p_T^{odd} and p_L^{odd}. Taking into consideration of the polarization angle α, $I^{2\omega}(M_i)$ is thus given by

$$I^{2\omega}(M_i)=(p^{even}\cdot\cos\alpha)^2+(p_T^{odd}\cdot\cos\alpha)^2+(p_L^{odd}\cdot\sin\alpha)^2$$
$$\pm2\cdot p^{even}\cdot p_T^{odd}\cdot\cos\alpha\cdot\cos\alpha\cdot\cos\varphi_T\pm2\cdot p^{even}\cdot p_L^{odd}\cdot\cos\alpha\cdot\sin\alpha\cdot\cos\varphi_L \qquad (2.3.7)$$
$$\pm2\cdot p_L^{odd}\cdot p_T^{odd}\cdot\sin\alpha\cdot\sin\alpha\cdot\cos\varphi$$

where α equals to 0° when the analyzer is set to P polarization, and 90° when the analyzer is set to S polarization. This is the general expression for the MSHG intensity. More specifically,

$$I^{2\omega}(M_I)=(p^{even}\cdot\cos\alpha)^2+(p_T^{odd}\cdot\cos\alpha)^2+(p_L^{odd}\cdot\sin\alpha)^2$$
$$-2\cdot p^{even}\cdot p_T^{odd}\cdot\cos\alpha\cdot\cos\alpha\cdot\cos\varphi_T-2\cdot p^{even}\cdot p_L^{odd}\cdot\cos\alpha\cdot\sin\alpha\cdot\cos\varphi_L \qquad (2.3.8)$$
$$+2\cdot p_L^{odd}\cdot p_T^{odd}\cdot\sin\alpha\cdot\sin\alpha\cdot\cos\varphi$$

$$I^{2\omega}(M_{II})=(p^{even}\cdot\cos\alpha)^2+(p_T^{odd}\cdot\cos\alpha)^2+(p_L^{odd}\cdot\sin\alpha)^2$$
$$-2\cdot p^{even}\cdot p_T^{odd}\cdot\cos\alpha\cdot\cos\alpha\cdot\cos\varphi_T+2\cdot p^{even}\cdot p_L^{odd}\cdot\cos\alpha\cdot\sin\alpha\cdot\cos\varphi_L \qquad (2.3.9)$$
$$-2\cdot p_L^{odd}\cdot p_T^{odd}\cdot\sin\alpha\cdot\sin\alpha\cdot\cos\varphi$$

$$I^{2\omega}(M_{III})=(p^{even}\cdot\cos\alpha)^2+(p_T^{odd}\cdot\cos\alpha)^2+(p_L^{odd}\cdot\sin\alpha)^2$$
$$+2\cdot p^{even}\cdot p_T^{odd}\cdot\cos\alpha\cdot\cos\alpha\cdot\cos\varphi_T+2\cdot p^{even}\cdot p_L^{odd}\cdot\cos\alpha\cdot\sin\alpha\cdot\cos\varphi_L \qquad (2.3.10)$$
$$+2\cdot p_L^{odd}\cdot p_T^{odd}\cdot\sin\alpha\cdot\sin\alpha\cdot\cos\varphi$$

$$I^{2\omega}(M_{IV})=(p^{even}\cdot\cos\alpha)^2+(p_T^{odd}\cdot\cos\alpha)^2+(p_L^{odd}\cdot\sin\alpha)^2$$
$$+2\cdot p^{even}\cdot p_T^{odd}\cdot\cos\alpha\cdot\cos\alpha\cdot\cos\varphi_T-2\cdot p^{even}\cdot p_L^{odd}\cdot\cos\alpha\cdot\sin\alpha\cdot\cos\varphi_L \qquad (2.3.11)$$
$$-2\cdot p_L^{odd}\cdot p_T^{odd}\cdot\sin\alpha\cdot\sin\alpha\cdot\cos\varphi$$

Applying Eq.2.3.8 - Eq.2.3.11 to Eq. 2.3.4, we obtain

$$C_L = 2\frac{k_L \tan(\alpha)\cos(\varphi_L)}{1+k_T^2+k_L^2\tan^2(\alpha)} \quad \text{and}$$

$$C_T = 2\frac{k_T \cos(\varphi_T)}{1+k_T^2+k_L^2\tan^2(\alpha)}, \tag{2.3.12}$$

where $k_L = \frac{p_L^{odd}}{p^{even}}$ and $k_T = \frac{p_T^{odd}}{p^{even}}$.

Equation 2.3.12 provides the L- and T-magnetic contrasts in a two-jump system as a function of polarization angle α including the ratios of magnitude and relative phases between non-magnetic and magnetic MSHG components. The significance for this study is: 1) both L- and T- components can be extracted from a two-jump hysteresis loop; 2) by fitting the contrast ratios as a function of analyzer angle, the information about the ratio of magnitudes and the relative phase can be obtained, which will provide deeper insight in the MSHG response.

2.4 Calculation of lensing effects

The Kerr lens effect is based on the optical Kerr effect, which is a third-order nonlinear effect that causes a change in the refractive index in the presence of intense laser beam. The focal length f can be roughly calculated by[100]

$$f^{-1} = \frac{4n_2 d}{\pi W^4} P, \tag{2.4.1}$$

where n_2 is the nonlinear refractive index, d is the thickness of the medium, P is the power, and W is the beam radius. For an un-focused beam, such focusing

effect is very small. For example, for a Gaussian laser beam with 800-nm wavelength, 100-fs pulse duration, 10-nJ pulse energy, and 2-mm radius shooting into a 7-mm thick Titanium doped sapphire crystal with $n_2=3e^{-20}$ m^2/W, the induced focal length is 598 km, which is negligible. However, such focusing effect becomes very strong for a focused beam.

Thermal lensing effects have been extensively studied as mentioned in Ch. 1.2.1. They have two major sub-effects: 1) temperature-induced refractive index change, and 2) thermal strain-induced refractive index change[68]. Empirical equations to roughly calculate the focal length have been developed, e.g., [101]

$$f \approx \frac{\kappa A}{P_a}\left(\frac{1}{2}\frac{dn}{dT}\right)^{-1}, \qquad (2.4.2)$$

where κ is the thermal conductivity, A is the area of the pump beam, P_a is the absorbed power, and dn/dT is the temperature variation in the index of refraction. A more accurate approach is to calculate the focal length by the optical pass deformation (OPD)[102-105], which can be written as

$$OPD = \int_0^l dndl, \qquad (2.4.3)$$

where l is the total length of light path in the medium and dn is the change of index along the light path. For a thermally induced dn, the temperature distribution in the medium needs to be calculated. Finite element analysis (FEA)

is the most accurate way to do the calculation, especially for the irregular shape like a Brewster-cut crystal (Fig. 2.4.1). The radially varying index in the medium leads to a radial change of OPD. That is the basic principle for the lensing effect and focal length calculation, not only for thermal but also for all other lensing effects. For example, the focal length of the population induced lensing effect can be calculated if the OPD's distribution in the Ti:Sapphire crystal is known.

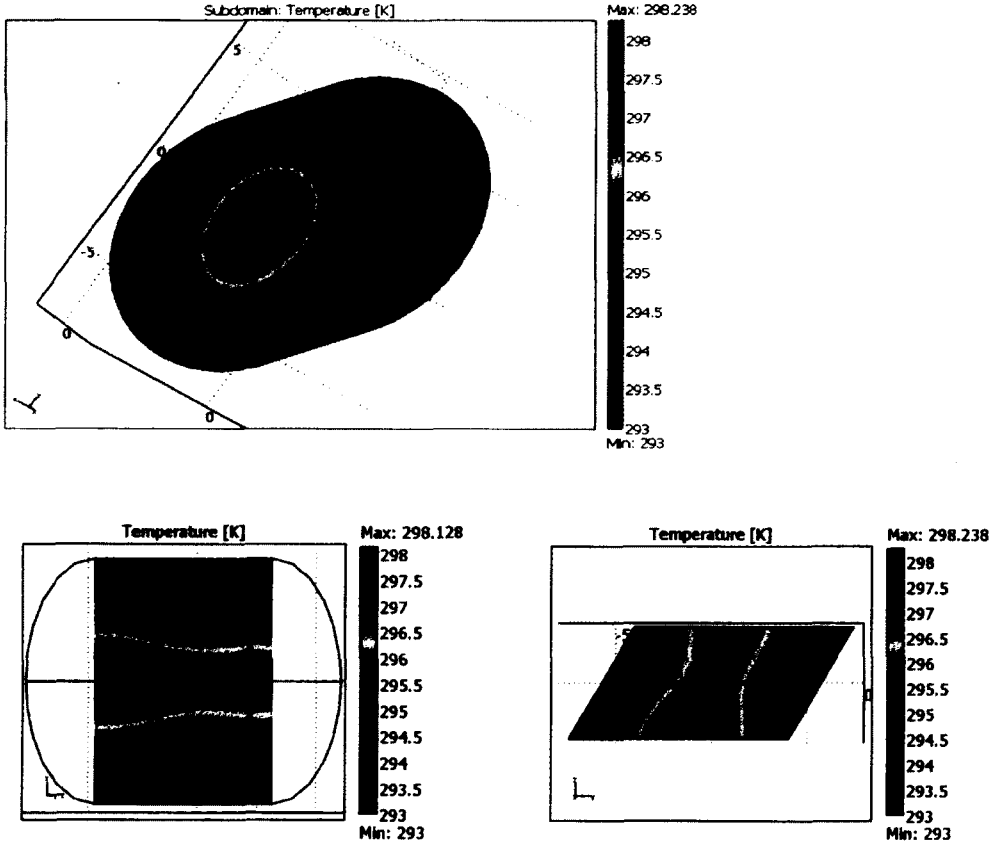

Figure 2.4.1 Temperature distribution of a Brewster cut Ti:Sapphire crystal pumped by a 20 W laser beam, simulated by FEA software COMSOL

2.5 Population induced strain in Ti:Sapphire crystal

Sapphire (Al_2O_3) has a hexagonal crystal structure , belonging to the trigonal crystal system with point group D_{3d}, space group $R\bar{3}c$, and Hermann-Mauguin notation $\bar{3}m$. The Al^{3+} ions occupy C_{3v} symmetry sites and 2/3 of the octahedral sites. The oxygen layer is perpendicular to the c axis[106,107]. Ti^{3+}:Sapphire is sapphire crystal doped by Ti^{3+} ions, which substitute the Al^{3+} sites and form TiO_6 complexes. The titanium ion has only one single *d* electron in the outermost shell while the remaining 18 electrons have the filled-shell configuration of a neutral argon atom. As the 3*d* electron electrostatically interacts with the electronic charges of six surrounding oxygen ions that are positioned at the corners of an octahedron, the 3d energy levels are split into higher energy T levels and lower energy E levels according to the orbitals' pointing direction[107]. The difference in energy corresponds to the energy of a green photon (approximately 500 nm). As a result, a green laser is used to pump 3d electrons of Ti^{3+}:Sapphire crystal from ground state to excited level. A coupling between the electron energy levels to the vibrational energy levels of the surrounding sapphire lattice makes the energy levels split further and makes a very wide emission band from 600 nm to 1200 nm[107-109]. The excited state has a different Ti-O equilibrium distance than the ground state, so that the volume of the TiO_6 complex in the ground and excited states are different. The coupling between the electron energy and vibrational energy determines the shape of the volume change[107]. It is known that the

volume of TiO_6 complex in the ground state is $V_{Ground} = 29.2 \pm 0.9 \overset{o}{A}^3$, and in the excited state $V_{Excited} = 41 \pm 0.9 \overset{o}{A}^3$, with volume change $\Delta V = 11.8 \pm 0.7 \overset{o}{A}^3$ [88].

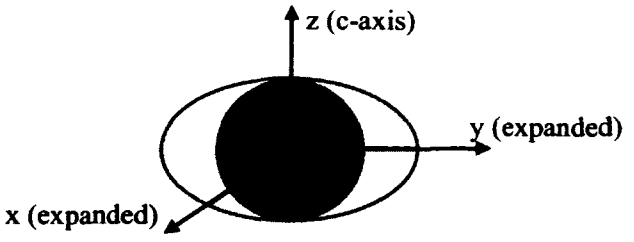

Figure 2.5.1 The excited state of TiO_6 complex expands as an ellipsoid

Note that because of the coupling of the Jahn-Teller mode, there is no effective deformation along the c axis. The deformation perpendicular to it leads to a change of ellipsoidally shaped volume with the expansion perpendicular to the c axis (Fig. 2.5.1)[107]. The strain per unit volume and per excited TiO_6 for an ellipsoid complex can be written as

$$\frac{s}{N} = \frac{\Delta V}{2}, \qquad (2.5.1)$$

where s is the strain, N is the number of exited Ti^{3+} ions per 1 cm^3. As $\Delta V = 11.8 \pm 0.7 \overset{o}{A}^3$, we obtain[88]

$$\frac{s}{N} = 5.9 \pm 0.4 \overset{o}{A}^3. \qquad (2.5.2)$$

2.6 Photoelastic effect for Ti:Sapphire crystal

The refractive index is determined by the permittivity (or dielectric constant), which are functions of the applied electric field and the stress on the crystal. The

change of refractive index caused by stress is called the photoelastic effect. In the absence of the biasing field E, if a uniaxial stress σ is applied to the crystal along the unique (optical) axis, the refractive index for a light wave, whose electric vector is in that direction, is given by [110,111]

$$n = n^0 + a\sigma + b\sigma^2 + \ldots, \tag{2.6.1}$$

where a, b are first order and second order stress constants. The relative dielectric impermeability tensor B_i at optical frequencies is induced and can be written as

$$B_i = \frac{1}{n_i^2} \quad . \tag{2.6.2}$$

It follows that the change of B_i can be written as

$$\Delta B_i = -(\frac{2}{n_i^3})\Delta n_i \quad . \tag{2.6.3}$$

ΔB_i under an applied strain s_i can be calculated by

$$\Delta B_i = p_{ij} s_i \quad , \tag{2.6.4}$$

where p_{ij} is the elasto-optical coefficient. In MKS unit system, the strain of a crystal produced by an optical field has the order of magnitude of 10^{-11}. With proper simplification by the symmetry of the crystal structure, the tensor matrix for Ti:Sapphire crystal can be written as[110]

$$\begin{pmatrix} \Delta B_1 \\ \Delta B_2 \\ \Delta B_3 \\ \Delta B_4 \\ \Delta B_5 \\ \Delta B_6 \end{pmatrix} = \begin{pmatrix} p_{11} & p_{12} & p_{13} & p_{14} & 0 & 0 \\ p_{21} & p_{22} & p_{23} & p_{24} & 0 & 0 \\ p_{31} & p_{32} & p_{33} & 0 & 0 & 0 \\ p_{41} & p_{42} & 0 & p_{44} & 0 & 0 \\ 0 & 0 & 0 & 0 & p_{55} & p_{56} \\ 0 & 0 & 0 & 0 & p_{65} & p_{66} \end{pmatrix} \begin{pmatrix} s_1 \\ s_2 \\ s_3 \\ s_4 \\ s_5 \\ s_6 \end{pmatrix} . \tag{2.6.5}$$

The number of tensor elements can be reduced with the following relations $p_{11} = p_{22}$, $p_{12} = p_{21}$, $p_{13} = p_{23}$, $p_{31} = p_{32}$, $p_{44} = p_{55}$, $p_{14} = -p_{24} = p_{65}$, $p_{41} = -p_{42} = \frac{1}{2} p_{56}$, $p_{66} = \frac{1}{2}(p_{11} - p_{12})$ [88,110]. Note that there are also six independent components when referred to arbitrary axes. The numbers 1, 2 and 3 correspond to x, y and z axis, respectively. The other three represent the deformation for fixed volume. As a result, in our case $s_1 = s_2 = s$ and $s_3 = 0$, because there is no strain (no expansion) along z-axis (c- axis) and it is equal for x and y directions. Also, $s_4 = s_5 = s_6 = 0$ because there is no deformation for fixed volume.

Given the elasto-optical coefficients of Ti^{3+}:Sapphire, the change of refractive index for light polarized in the same direction can be calculated by

$$\begin{aligned} \Delta n_1 &= -\frac{n_1^3}{2}(p_{11} + p_{12})s \\ \Delta n_2 &= -\frac{n_2^3}{2}(p_{21} + p_{22})s \\ \Delta n_3 &= -\frac{n_3^3}{2}(p_{31} + p_{32})s \end{aligned} \quad . \qquad (2.6.6)$$

Since $n_1 = n_2$ and $p_{12} = p_{21}$, $p_{11} = p_{22}$, $p_{13} = p_{23}$, the Δn in x and y directions (normal to c-axis) are the same and the Δn along c-axis can be calculated by

$$\Delta n_3 = -n_3^3 p_{31} \frac{s}{N} . \qquad (2.6.7)$$

So far, the lensing effect, population induced strain, and strain induced refractive index change are discussed. With the elasto-optical coefficients and the

distribution of population density, one can calculate the focal length due to upper level population. However, the elasto-optical coefficients of Ti^{3+}:Sapphire are not available and researchers have used the data of Cr^{3+}:Sapphire instead. One goal of this dissertation is to determine experimentally these coefficients.

Chapter 3: Experimental Section

Nonlinear optics has been explored shortly after the demonstration of the first laser by Peter Franken et al. at the University of Michigan[112] because the strong optical field of the laser beam induces high enough polarization density in a material. The Q-switch technique allows more energy to be accumulated in the laser upper level and a pulsed output, resulting in short pulses (normally 10 nanoseconds) and a higher peak power, which are more favorable for nonlinear optical effects. The mode-lock technique can shorten the pulse width down to the range of less than 10 femtoseconds (fs) to several picoseconds (ps)[113]. If a mode-locked oscillator is combined with a CPA, the output beam could have very short pulse-width with large energy and thus huge peak power and intensity, which is most favorable for nonlinear optical effects[114]. My experiments are based on such system.

3.1 Ultrafast laser system and Chirped-Pulse-Amplifier

3.1.1 Mode-lock technique and Chirped-Pulse-Amplifier

The longitudinal modes of the laser cavity are standing waves with discrete frequencies allowed to oscillate in the resonant cavity[113]. For example, in a Fabry–Pérot cavity (parallel plane-mirror cavity), the distance of mirrors L can be expressed as $L = q\lambda/2$, where λ is the wavelength and q is an integer known as the

mode order. If all the allowed modes operate with a fixed phase between each other, the laser is called mode-locked. Such lasers have very short pulses which are like intense burst[113].

The most successful scheme to mode-lock a laser is called Kerr-lens mode-locking (KLM) technique[115]. As mentioned in Chapter 1, the optical Kerr effect is a third order nonlinear effect, which causes a change in the refractive index in the presence of intense light such as a laser beam. The variation of refraction index is proportional to the local intensity of the laser beam, which often has a Gaussian distribution, resulting in the self-focusing, self-phase modulation and the Kerr-lens mode-locking effects[115]. The optical Kerr-lens effect causes high-intensity beam (mode-locked and pulsed beam) and low-intensity beam (continuous wave beam with random phase) to have different focal lengths. By carefully designing the laser cavity to be favorable for the high-intensity beam by utilizing the Kerr-lens effect, only the high-intensity beam composed of in-phase longitudinal modes can oscillate in the cavity, thus the laser is mode-locked.

Although ultra-short pulses generated by a mode-locked oscillator have very high peak power, the energy contained in each pulse is quite small. A CPA can amplify the pulse energy from nanojoules to several joules. It is used in most of

the world's powerful laser systems. In a CPA, the ultra-short pulses are first stretched out temporally using a grating pair or a dispersive medium so that the low-frequency and high-frequency components are separated temporally (also called chirped), and thus the pulses have a longer duration than the original ones by a factor of 10^3 to 10^5. This pulse stretching process makes it possible that each pulse can contain very high energy without damaging the gain medium or other optics because of the sufficiently low intensity due to the longer pulse duration. The stretched pulses then become amplified by the gain medium by a factor of 10^6 or more, normally. At the last stage, the pulses are re-compressed back to their original pulse width by another grating pair with opposite arrangement or a negative dispersion medium, introducing the reversal process of the stretching. As a result, the peak power of the pulses is amplified by orders of magnitude[114]. Figure 3.1.1 shows the different stages in a CPA.

There are two types of amplifiers: regenerative amplifier and multi-pass amplifier, both of which are mostly based on titanium doped sapphire crystals. The regenerative amplifier is composed of gain medium in an optical resonator together with an optical switch, and is used for relative lower power pulses yet with a very large overall amplification factor (around 10^6). The multi-pass amplifier is suitable for higher energy pulses (more than mJ level) with a relative lower amplification factor with low amplified spontaneous emission (ASE)[116].

The multi-pass amplifier normally has a simpler setup, which arranges the pulses going through the gain medium several times (mostly 2 to 8 passes) by a set of mirrors[114]. To achieve highest peak powers, most commercial CPA systems contain more than one amplifier. A regenerative amplifier as pre-amplifier followed by a multi-pass amplifier is the prevailing configuration[114].

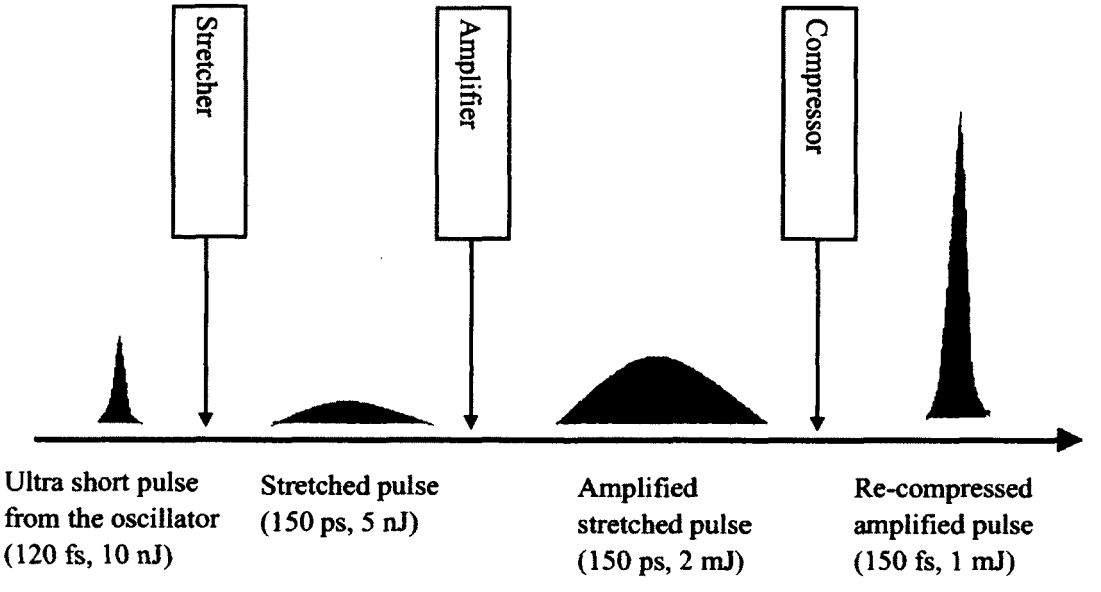

Figure 3.1.1 Specs of the laser pulse in different stages of a typical CPA

In a CPA system, a pump beam with high fluence or energy density is always desired, because the pumping fluence is critical for the single-pass amplification rate. However, due to the Gaussian distribution of the beam profile, the fluence in the center part of the pump beam is much higher, which may lead to crystal

damage, while the average fluence may not be high enough to guarantee sufficient gain. Furthermore, high-energy pump lasers unavoidably have hot spots in the central area of the laser beam and have a multi-mode output, which makes the situation worse. In the following, a spatially and temporally homogenized pumping system is designed for a 5-pass, 30-Hz, terra-watt CPA. This design protects the Ti:Sapphire crystal and generates up to 130-mJ pulses with a total amplification rate of 300 and a conversion efficiency of 20%.

3.1.2 Amplification in a Chirped Pulse Amplifier

For general laser media, the small signal gain is given as $g_0 = N \cdot \sigma_{emission}$, where $\sigma_{emission}$ is the stimulated emission cross section and N is the excited state population which is proportional to the pump fluence (unit: J/cm^2). If the seed beam pulse intensity is close to the saturation intensity, the gain is given by $g = \frac{g_0}{1 + J/J_{sat}}$, where J is the fluence of the seed beam and J_{sat} is the saturation fluence[117]. If the round-trip losses, gain saturation, and the change of gain are taken into account, multi-pass amplifiers' performances can be best described by the model of Frantz and Nodvick[118].

$$J_{out}^{(p)} = J_{sat} \ln\left(1 + G_0^{(p)}\left\{\exp\left[\frac{J_{in}^{(p)}}{J_{sat}}\right] - 1\right\}\right), \qquad (3.1.1)$$

where $G_0^{(p)} = \exp[J_{store}^{(p)} / J_{sat}]$ is the small signal gain for pass p. $J_{in}^{(p)} = \Gamma J_{out}^{(p-1)}$ is the seed beam's fluence going into the crystal and Γ is the loss coefficient per

pass. $J_{store}^{(p+1)} = J_{store}^{(p)} - J_{out}^{(p)}$ is the stored energy. $J_{store}^{(p)} = \eta J_{abs} \times (\lambda_p / \lambda_s)$, where η is the coupling coefficient and J_{abs} is the pump fluence absorbed by the crystal.

From Equation 3.1.1 we know that higher pump fluence going into the crystal is beneficial to achieve higher gain, which is independent of the general gain in the laser medium for the specific multi-pass model. Meanwhile, the pump fluence must not go beyond the damage threshold (f_{damage}), which is 5 J/cm^2 for Ti:sapphire crystal[117,118]. In most cases, because of the nonuniformity of the transverse energy distribution in the pump beam, the pump fluence in some parts of the beam approaches the damage threshold while the fluence in other parts and the average fluence remain low. This limits the total performance of the amplifier. The situation is much worse for high energy pulse pump lasers because they always have hot spots in the beam.

To clearly explain the problem and how it is solved, a parameter is defined as

$$K = \frac{f_{peak}}{f_{average}}, \qquad (3.1.2)$$

which indicates the ratio of the peak fluence (f_{peak}) to the average fluence ($f_{average}$). For single mode Gaussian beam, the K value is normally less than 2.7. If the edge part of the beam is neglected, where only a tiny portion of the energy is contained, K is less than 2 (For the beam with Gaussian distribution shown in

Fig. 3.1.2, K = 1.8650). This means that the average pump fluence must not go beyond $\frac{f_{damage}}{K} = \frac{5}{1.865} J/cm^2$ for the safety of the crystal to accommodate the peak energy density at the center in engineering designs. Actually, the real beam is far more complex, composed of many high-order TEM modes and spikes made by hot spots as shown in Figure 3.1.5 (refer to Fig. 4.1.4). The K value for this beam (Quanta Ray, 30Hz, 800mJ/pulse) is 4.2974, which is much worse than a single-mode Gaussian beam. To avoid damage of the crystal, the total pump fluence has to be reduced by a factor of 4.2974 to accommodate the peak energy density at the spikes. As a result, the pump energy density and gain decrease. Therefore, the pump beam needs to be homogenized to lower the K value.

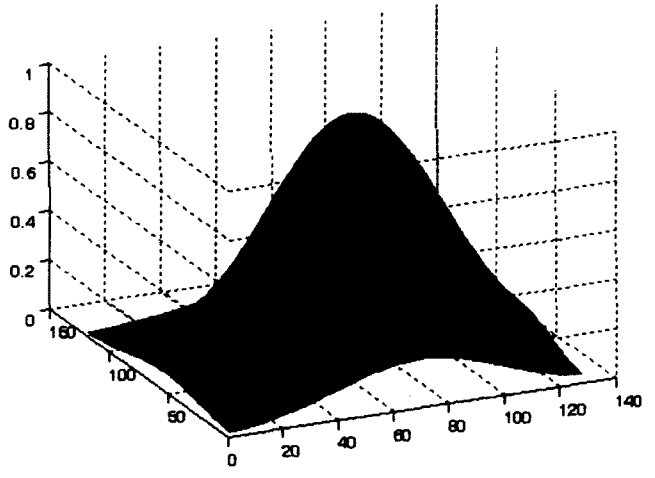

Figure 3.1.2 Energy distribution of a single mode Gaussian beam

3.1.3 Spatial homogenization of pump beam

The high energy pump beam is first split into two parts so that the crystal can be pumped from both sides. This guarantees a high fluence along the light path in the crystal while it decreases the light intensity at the end surface, where damage most likely happens. The *K* value is decreased to 2.6902 by this method. Figure 3.1.3 shows the pump fluence along the light path. The maximum fluence at both ends (red line) decreases by about 30% for only one end pumping (blue line).

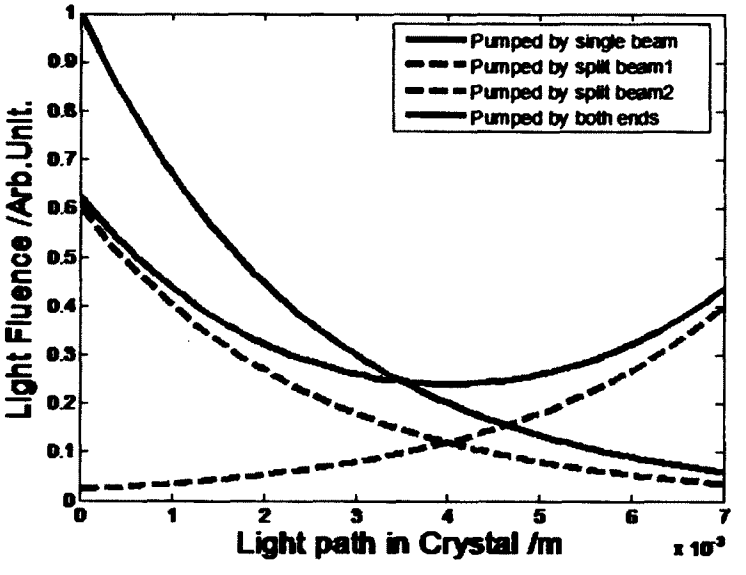

Figure 3.1.3 Fluence distribution along the light path in the Ti:sapphire crystal. Pumping from both sides (red) is more homogeneous than from single side (blue)

To lower the *K* value further, especially to erase the danger of damage by hot spots in the beam, the beam in each direction is split again. The basic idea is illustrated in Figure 3.1.4. The beam is split into two parts, each with lower

fluence than the original one. These parts are overlapped in the transverse direction by two mirrors. Then, they are recombined on the crystal with the hot spots spread out. This step decreases the *K* value further to 2.3234, which is much better than the original value of 4.2974. Figure 3.1.5 shows the original beam profile and the beam profile after recombination. The energy is even and the spikes are less distinct for the recombined beam. Note that in the setup, the beam energy is not split equally for some technical reasons. The ratio is 4 to 6 and 3.5 to 6.5 for the first and second split, respectively. Technically, if the beam is split into equal parts, the K value could decrease further to 1.8866, which is close to the K value pumped by a single mode Gaussian beam.

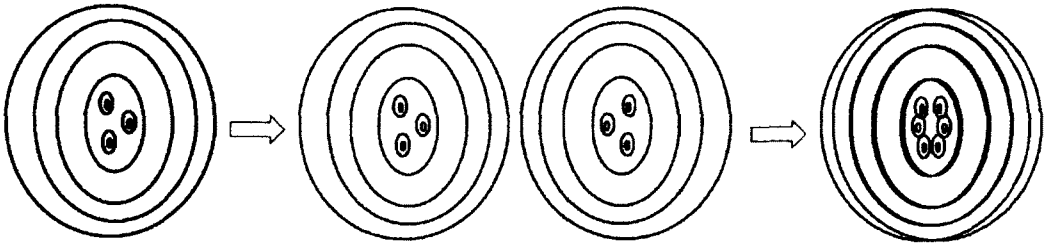

Figure 3.1.4 Split, reverse and recombine to spread the hot spots

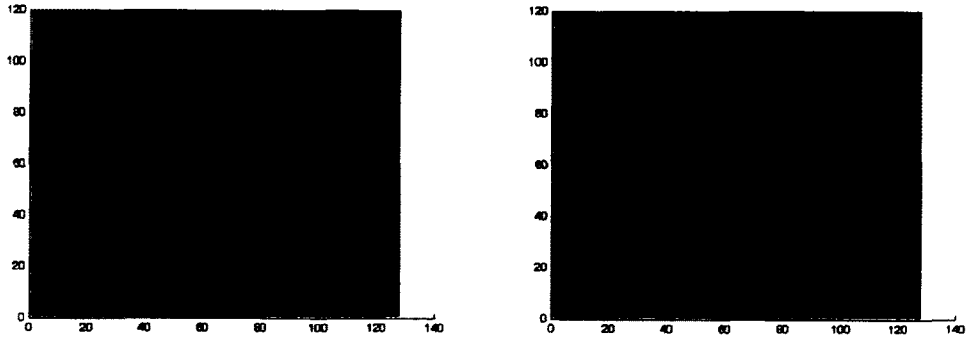

Figure 3.1.5 Real beam profile before and after recombination

In conclusion, Figure 3.1.6 shows the *K* values in various situations and the progress made by my design. A *K* value of 2.7 is commonly used in engineering calculation[119], 1.8650 is for single mode Gaussian beam, 4.2974 is the original value of the pump beam, and 2.3234 is the value after optimization. My result achieves a huge improvement over the original pump beam and is better than the common value in commercial CPA systems.

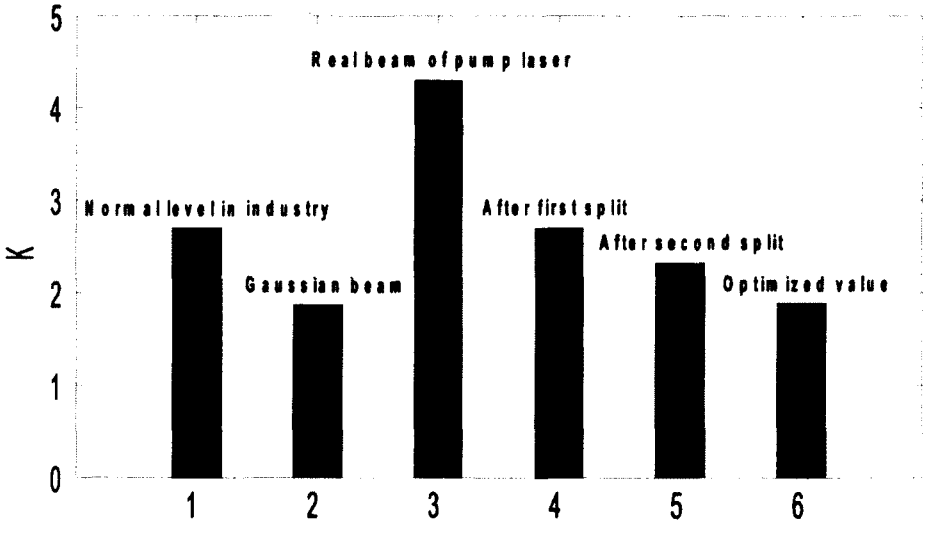

Figure 3.1.6 K values in various situations

3.1.4 Temporal homogenization of pump beam

Unlike continuous wave (CW) lasers, for pulsed lasers in the range of microsecond to nanosecond, the damage threshold is rated as fluence or energy density with the unit of J/cm^2, instead of power density with the unit of W/cm^2.

There is no certain relationship to describe the change of damage threshold with the change of pulse duration. Based on the experience in engineering and technical calculations, the damage threshold varies as a function of the square root of the pulse duration[120]. For example, if the damage threshold for an optical element is 5 J/cm^2 for 10 nanosecond pulses, it changes to 50 J/cm^2 for 1000 nanosecond pulses, which means it can withstand 10 times more energy. Therefore, my basic idea to temporally homogenize the pump beam is to extend its pulse duration. In practice, before the two pump pulses on each side are recombined, I apply delays between them, which are 5 and 3 nanoseconds, respectively. The original pump pulse duration is 10 ns (Fig. 3.1.7 blue line). After the delays are applied, the durations change to 13.5 (Fig. 3.1.7 green line) and 12 ns (Fig. 3.1.7 red line), which means the crystal can withhold 16% and 10% more energy than it does without the delay. Since the population lifetime for Ti:Sapphire is about 3 microseconds, which is much longer than the pulse duration, the change in pump pulse duration will not affect the conversion efficiency.

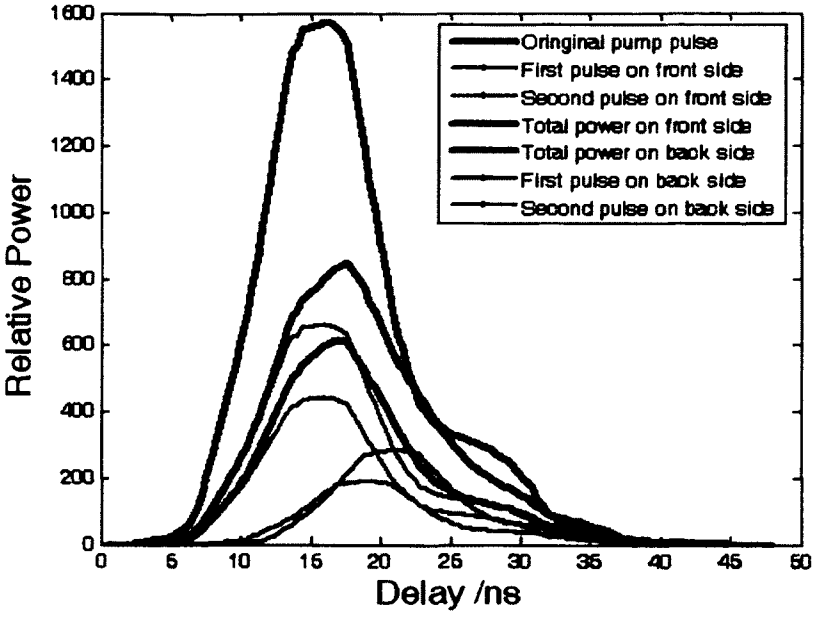

Figure 3.1.7 Pump pulse duration with (red and green lines) and without (blue line) delay

To summarize, split, reversion, recombination and delay are applied to optimize the pump configuration in a multi-pass CPA laser amplifier system (Fig. 3.1.8). Along with the compensation of lensing effect for seed beam, this setup generates up to 130-mJ pulses with a total amplification rate of 300 and a conversion efficiency of 20%, which is among the highest for CPA systems.

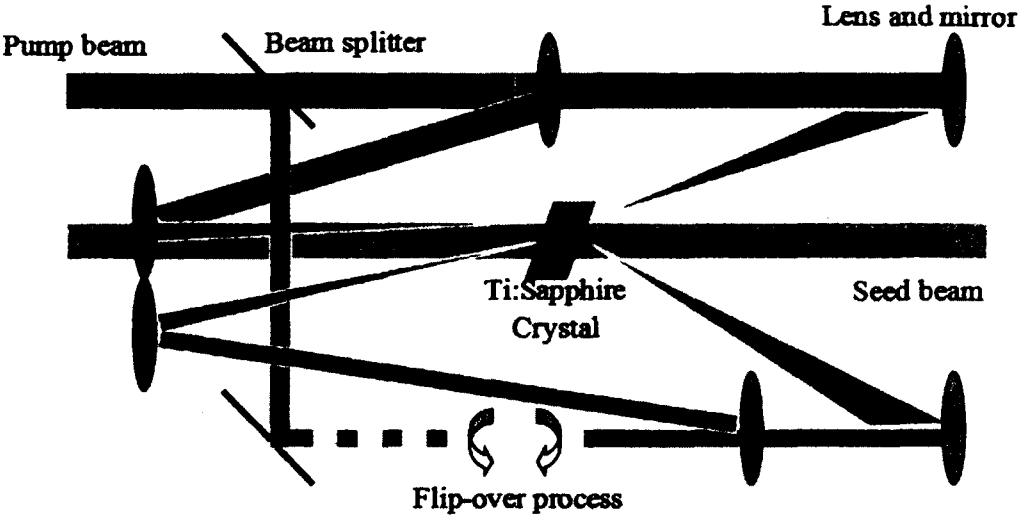

Figure 3.1.8 Overall layout of the pump scheme

3.2 Experimental setup for nonlinear magneto plasmonic

3.2.1 Configuration of lasers

A system composed of several commercial lasers is used in the study of NMP. A Ti:Sapphire mode-locked laser pumped by a green continuous-wave (CW) laser generates ultra-short pulses with the duration of about 120 fs and the rep rate of 80 MHz, which is called seed beam. A synchronization system converts the rep rate of the seed beam to 1 kHz and synchronizes it with a pump laser beam, which is generated by a Q-switch laser. A pulse stretcher composed of a grating pair and a spectral mask, a regenerative amplifier, a 2-pass amplifier and a compressor composed of another grating pair make up the whole CPA. Finally,

the output beam has a pulse energy of 2 mJ and a pulse width of 2 picosecond (Fig. 3.2.1).

Because the surface plasmon can only be excited by P-polarized light under Kretschmann-Raether configuration (refer to Ch.3.2.2), a half-wave plate is used to convert the beam from S- to P-polarized. The beam diameter is decreased from 12 mm to 2 mm by a telescope, in order to have a higher light field intensity and to fit the size of the rest of the data gathering setup. It is critical to use a collimated beam because it has advantages over a focused beam for the following reasons: 1) the excitation of surface plasmon (SP) is very sensitive to the incident angle, while the incident angle for a focused beam has a larger span; 2) for a focused beam, the beam diameter varies much with a tiny change in position, which could bring very large errors for SHG signal in the experiments; 3) to guide the very weak second harmonic signal to the detector (photo multiplier tube), a collimated beam is much easier than a focused beam.

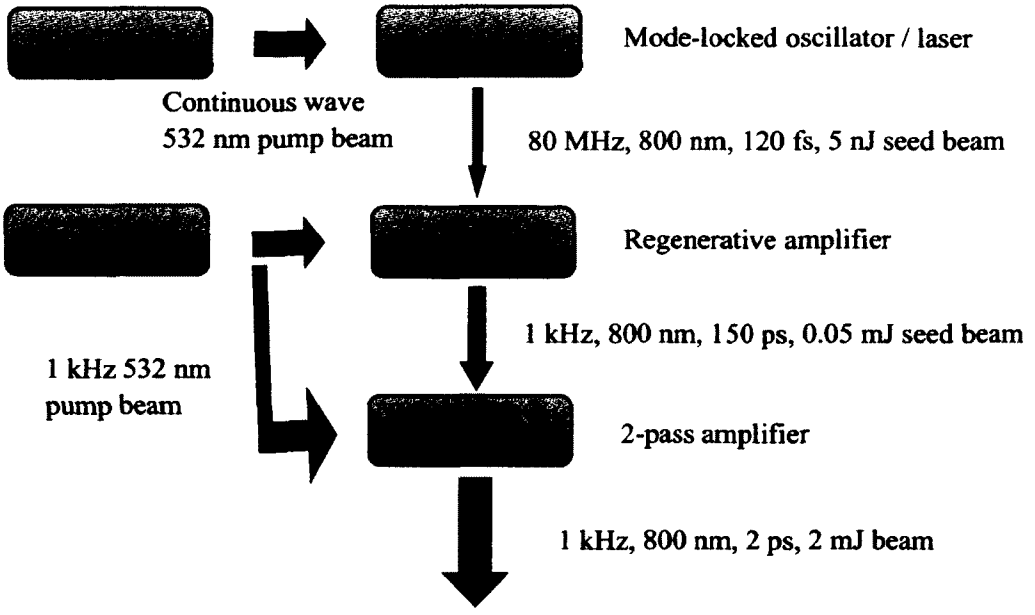

Figure 3.2.1 Picosecond laser system for surface plasmon excitation and second harmonic generation

3.2.2 Excitation of surface plasmon

The SP is an electromagnetic wave performing coherent fluctuations that propagate along a metal-dielectric interface. By solving Maxwell's equations for the electromagnetic wave at an interface between two materials with permittivity (dielectric constant) ε_1 and ε_2 (ε_1 is for metal and ε_2 is for the dielectric) with the appropriate continuity relation and the boundary conditions, the dispersion relation (ω as a function of k) for a wave propagating on the surface is[37]

$$k_x = \frac{\omega}{c}\left(\frac{\varepsilon_1\varepsilon_2}{\varepsilon_1+\varepsilon_2}\right)^{1/2}, \qquad (3.2.1)$$

where c is the speed of light, k is the wave vector and ω is the frequency of SP. The SP behaves like a photon at low k, where $\omega = c \cdot k$. As k increases, the dispersion relation bends over and reaches an asymptotic limit called the "surface plasmon frequency". As a result, the dispersion curve lies to the right of the light line $\omega = k \cdot c$. The surface plasmon frequency is the asymptote of this curve, and is given by

$$\omega_{SP} = \omega_P / \sqrt{1+\varepsilon_2}\,, \tag{3.2.2}$$

where ω_p is the bulk plasma frequency which can be given by

$$\omega_P = \sqrt{\frac{ne^2}{\varepsilon_0 m^*}}\,, \tag{3.2.3}$$

where n is the electron density, e is the charge of the electron, m^* is the effective mass of the electron and ε_0 is the permittivity of free-space. In conclusion, the surface plasmon frequency is determined by the properties of the metal and the dielectric constant of the dielectric (ε_2).

There are several methods to excite a surface plasmon. One can use an electron beam to penetrate a solid and transfer momentum and energy to the electrons of the solid and excite SP. Localized SP can be excited by sending light on a rough surface built up of nanostructures or particles. A metal grating or corrugated structure hit by a light beam can also excite SP because the change of the light wave vector by the grating meets the dispersion relation of the SP (Eq. 3.2.1) and thus can couple the photons to SP[37]. The most convenient method for metal film

structures is the Kretschmann-Raether configuration[37] as shown in Figure 3.2.2, which also can be treated quantitatively.

As mentioned above, the dispersion relation of SP lies to the right of the light line ($\omega = c \cdot k$) which means that the surface plasmon has a longer wave vector than the light wave of the same energy propagating along the surface. Therefore, a coupler is needed to match the wave vectors of light and SP. In Kretschmann-Raether configuration, an iron film is attached to a quartz prism, which increases the momentum of light from $\hbar\omega/c$ to $(\hbar\omega/c)\sqrt{\varepsilon_0}$. The projection onto the surface is

$$k_x = \sqrt{\varepsilon_0}\frac{\omega}{c}\sin\theta, \qquad (3.2.4)$$

where $\sqrt{\varepsilon_0}$ is the refractive index of quartz which equals 1.5, and θ is the incident angle. The wave vector (Eq. 3.2.4) satisfies the dispersion relation for SP at the metal-dielectric interface with permittivities ε_1 of the metal and ε_2 of the dielectric (Eq. 3.2.1), and the SP is excited at that interface (Fig. 3.2.2). Because the incident angle θ corresponding to the matching of the wave vectors is always beyond the total reflection angle and the reflection is attenuated due to the coupling of the light to the SP, this method is also called attenuated total reflection (ATR) method.

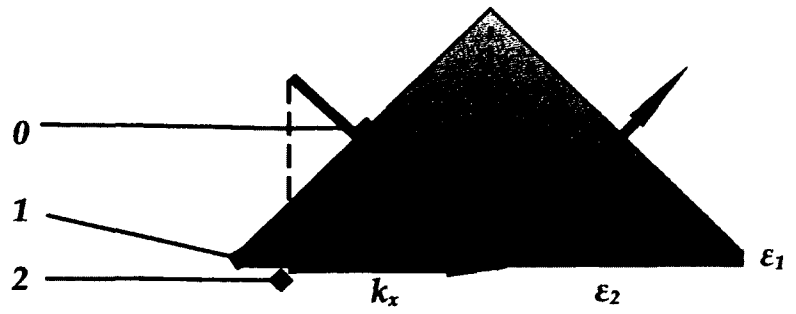

Figure 3.2.2 Kretschmann-Raether configuration: 0 is the coupler made of the quartz, 1 is the metal film, and 2 is air

3.2.3 Setup for data gathering

The experimental setup for data gathering is shown in Figure 3.2.3. A quartz prism is used for the Kretschmann-Raether configuration to excite the SP. The MgO substrate is attached to the prism by index matching oil. A data gathering system including chopper, boxcar, lock-in amplifier, photon multiplier tube (PMT), and polarizers with 1:10000 extinction ratios enables detection of the small MSHG signal. An infrared (IR) filter is placed before the prism to filter out the blue light generated from the laser system and the optics, and a blue filter is placed before the PMT to block the fundamental 800 nm light. An interface bus (GPIB)-controlled split-coil electromagnet provides an external magnetic field. A set of Lab View programs are written on a PC to control the rotation motor and magnet, and to gather the data through GPIB cables.

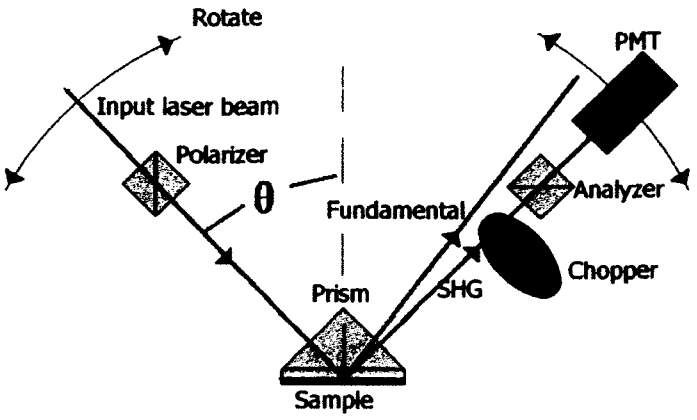

Figure 3.2.3 Experimental setup of nonlinear magneto plasmonics

One very tricky design is the rotation stage. As Figure 3.2.3 shows, in order to get the signal as a function of incident angle, not only the incident beam changes position, but also the detectors need to rotate accordingly, which makes the alignment extremely complex. A retroreflector is used to solve this problem. A retroreflector reflects light back to its source direction and keeps the incident and output beam parallel to each other. The retroreflector is composed of a prism carrying the sample and a prism with thick silver coating as a reflector (Fig. 3.2.4). Under such configuration, one only needs to rotate the retroreflector to change the incident angle and keep the rest of the optics fixed.

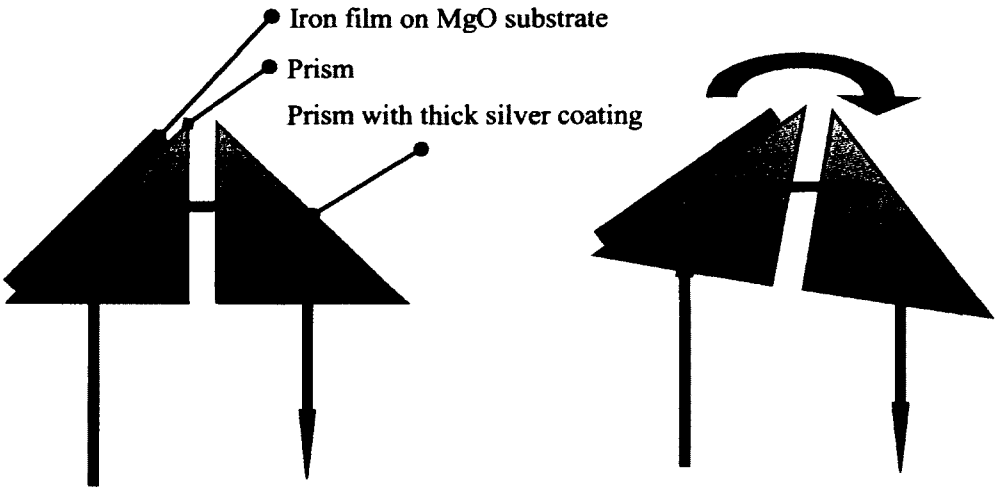

Figure 3.2.4 Retroreflector

3.3 Experimental setup for Photoelastic effect

3.3.1 Configuration of lasers

The research of photoelastic effect originates from the design of a table top Ti:Sapphire multi-pass CPA system. I discovered that the seed beam pumped by a synchronized pump beam has a much shorter focal length than a CW beam under the same condition. A lensing effect must occur that happens in phase with the pump beam, which is different from the average thermal effect. The configuration of the laser is straightforward (Fig. 3.3.1) and similar to a real CPA system. The seed beam generated from a mode-locked laser goes through a Brewster cut, 7 mm in light path and 0.25% Ti^{3+} doped sapphire crystal. The crystal is cooled by a 50 W thermoelectric cooling unit with additional circulating

water to keep the side boundary temperature at 20 ^{0}C, which is the real cooling condition when the crystal works as the gain medium in a CPA. A very powerful Q-switch laser which generates up to 800 mJ energy per pulse is used as the pump laser. The pump beam is focused to be 4 mm in diameter, and the crystal is pumped from both sides. The seed beam going through the crystal is studied.

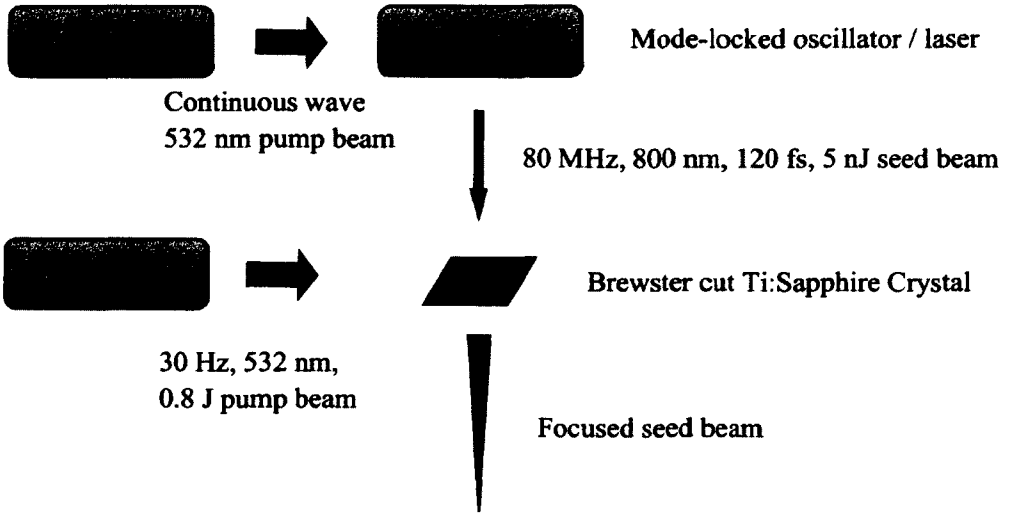

Figure 3.3.1 The arrangement of lasers in the study of photoelastic effect

As elaborated in the theoretical section (Ch. 2.5), the photoelastic effect is caused by the strong pump laser pulses and happens in the time scale of microsecond. The time-dependent measurement of this very fast lensing effect is difficult. Firstly, it is different from the average thermal lensing effect, which can be directly measured by a CW laser beam going through the laser crystal. Secondly, the pump-probe method is not suitable either, because its applicable range is between hundreds of femtoseconds to hundreds of picoseconds limited by the

actual delay applied between the pump and probe beams. Thirdly, the test beams with different delay will differ in intensity due to different amplification factors. This makes it difficult to determine the focusing condition from a detection device such as a CCD camera because it often has the saturation problem when the energy and focal length change. Using different attenuators destroys the base for comparison.

3.3.2 Measurement of the focal length

In this study, an experimental setup is designed to catch this very fast lensing effect. For a Gaussian distributed laser beam, the power contained within the radius r is[116]

$$P(r) = P \cdot [1 - \exp(\frac{-2r^2}{w^2})], \qquad (3.3.1)$$

where P is the total power, r is the radius of the iris, and w is the beam radius. Having determined the power with and without the iris, one can obtain w by

$$w = \left(\frac{-2r^2}{\ln(1 - \frac{P(r)}{P})} \right)^{1/2}. \qquad (3.3.2)$$

Here, the actual value of the power is not important anymore. The ratio of the signal strength is used instead, as long as the signal strength represents the power. This allows the use of a photodiode as the measuring device. Furthermore, the change of signal strength due to the time delay dependent amplification rate is canceled out.

Now that the beam radius w at the iris is known, the task becomes to determine the relation between focal length of the crystal (f_c) (Fig. 3.3.2) and w. To get this geometrical relation, an approximation is made which treats the initial laser beam as a parallel beam instead of a Gaussian one. For a parallel beam, knowing w, one can calculate the beam radius at the lens by

$$w_l = \frac{w \cdot f}{L - f}, \tag{3.3.3}$$

where f is the focal length of the lens and L is the distance between the lens and the iris. Similarly, one can further obtain the focal length of the crystal by

$$f_c = \frac{w_c \cdot d}{w_c - w_l}, \tag{3.3.4}$$

where w_c and w_l are the beam diameters at the crystal and the lens, respectively, and d is the distance between the crystal and the lens. From this relationship the focal length of the crystal can be obtained, as long as the ratio of the signal strength with and without the iris is known (Eq. 3.3.2).

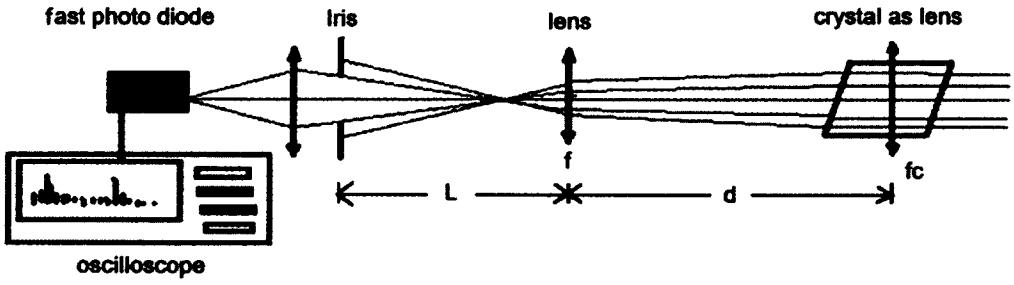

Figure 3.3.2 Data gathering system for the very fast photoelastic effect

In this experiment, I use a fast photodiode to measure the intensity of the test beam pulses as the relative power, and set L=165 cm, f=15 cm, and d=200 cm. A lens with focal length of 6 cm is placed in front of the photodiode, which guarantees that all the signals are collected by the diode.

I apply the rules for the propagation of a focused Gaussian beam which takes the focal point shift into account to test whether the approximation above is accurate. According to the ABCD matrix formula, the laser beam at the iris can be expressed as $Q = Z + iZ_0$, where $Z_0 = \pi w^2 / \lambda$ is the Rayleigh length. In the same way, the laser beam at the crystal can be written as $q = z + iz_0$. The ABCD matrices employed in this calculation are $M_1 = \begin{bmatrix} 1 & 0 \\ -\frac{1}{fc} & 1 \end{bmatrix}$, $M_2 = \begin{bmatrix} 1 & d \\ 0 & 1 \end{bmatrix}$, $M_3 = \begin{bmatrix} 1 & 0 \\ -\frac{1}{f} & 1 \end{bmatrix}$, and $M_4 = \begin{bmatrix} 1 & L \\ 0 & 1 \end{bmatrix}$. The overall transfer matrix is $M = M_4 \bullet M_3 \bullet M_2 \bullet M_1 = \begin{bmatrix} A & B \\ C & D \end{bmatrix}$ and $Q = \frac{A \cdot q + B}{C \cdot q + D}$ [121]. Figure 3.3.3 shows the simulation result for both methods. As long as the focal length of the crystal is larger than 5.5 meters (about the Rayleigh length of the seed beam), the error is below 5% (for example, when the focal length is 5.5 meters, the values of beam radius at the iris calculated by each method are 0.5652 cm and 0.5397 cm respectively). The approximated calculation is thus considered accurate.

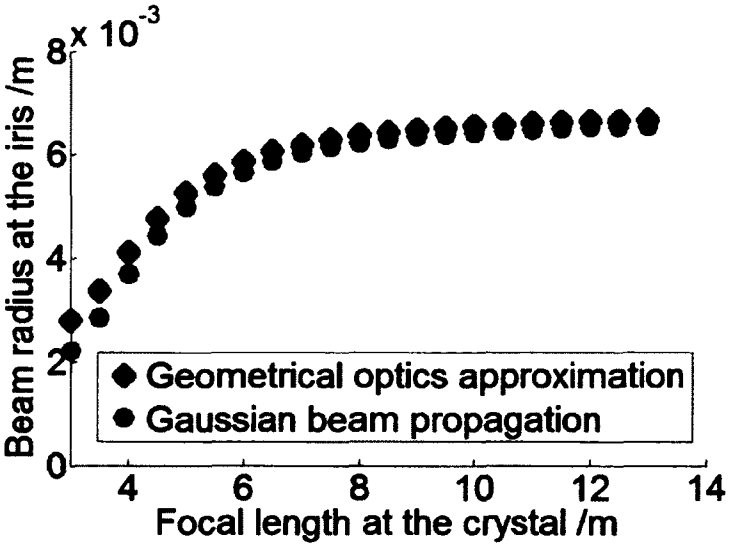

Figure 3.3.3 Comparison between geometrical optics approximation (diamond) and Gaussian beam propagation (circle) calculations

3.3.3 Trace the fast signal

The time-dependent measurement is carried out by a fast photodiode and a gigahertz oscilloscope. This measurement provides a temporal resolution of one nanosecond and can catch every pulse from the 80 MHz seed beam. Each pulse represents a state of certain delay with respect to the pump laser. Therefore, the time-dependent data is actually made up by many pulses with different delay.

The original data is shown in Figure 3.3.4 a. It is composed of many pulses and shows the effect of the pump beam. The seed beam has the strongest pulse when the time delay is zero and its energy decreases over time all the way to its original state. This is mostly due to the amplification effect by the pump beam. This effect can be canceled out using an iris. Note that due to the jitter effect of

the oscilloscope sampling frequency, there is a periodic fluctuation in the signal strength (Fig. 3.3.4 b). Such noise can be removed by processing it through a 50-point average window in MATLAB.

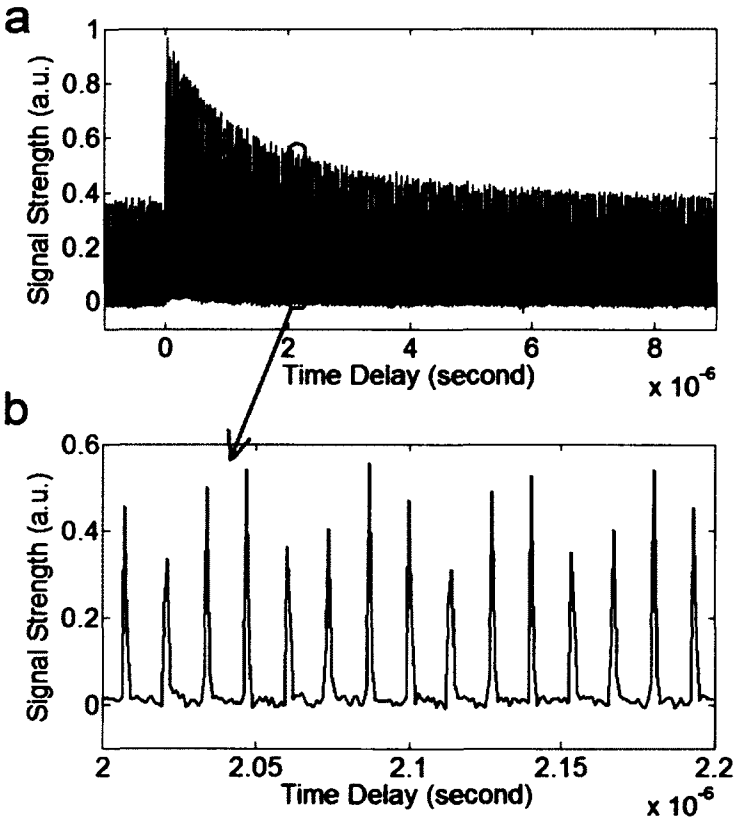

Figure 3.3.4 The oscilloscope catches every pulse from the seed beam

Chapter 4: Population-Induced Photoelastic Lensing Effect

In this chapter, I present the measurement results of the fast photoelastic lensing effect induced by the upper level population in a Ti:Sapphire crystal. By analyzing the measured focal length and the real pump beam profile taken by a CCD camera, I determine the opto-elastic tensor of Ti:sapphire crystal. The tensor is very important to evaluate the population-induced photoelastic lensing effect.

4.1 Measurement of photoelastic lensing effect

The crystal I use in this study is a Brewster cut, 7 mm in light path and 0.25% Ti^{3+} doped sapphire crystal with the absorption coefficient of 4.1 cm^{-1} ± 20%. The pump beam is focused to 4 mm in diameter. The crystal is pumped from both sides. I use the seed beam with 800 nm wavelength and a repetition rate of 80 MHz directly from the oscillator (Tsunami, Spectra-Physics) as the test beam and the pump beam with 532 nm wavelength and a repetition rate of 30 Hz (Quanta-Ray, Spectra-Physics). The fast photodiode provides a temporal resolution of 1 nanosecond. I use 50 W thermoelectric cooling units and additional circulating water to keep the temperature of the Ti:sapphire crystal at 20 °C.

The original data taken from an oscilloscope triggered by the pump laser is shown in Figure 3.3.4. The envelope of the pulse train shows a clear profile of amplification by the pump. As described in Ch.3.3.2, by taking the ratio of the signal with and without an iris, the amplification of the test beam can be canceled out. Furthermore, this ratio will be used to calculate the focal length (Eq. 3.3.2 -3.3.4).

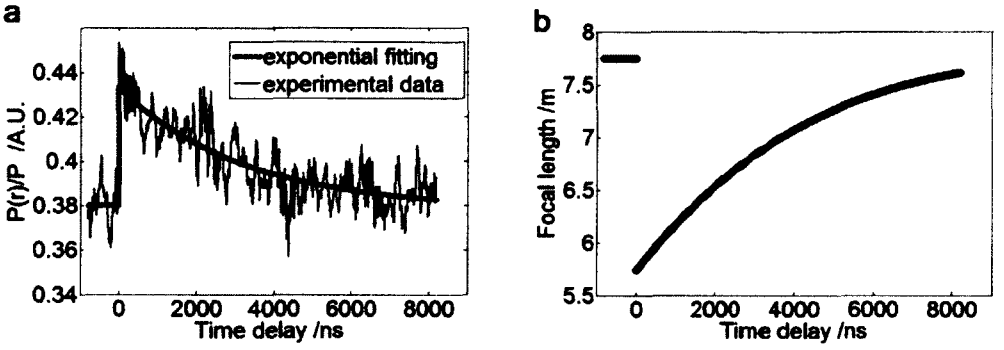

Figure 4.1.1 Time dependent measurement of the lensing effect (pump energy is 500 mJ), (a) original data and the fitted curve, (b) calculated focal length based on the fitted curve

Figure 4.1.1 shows the ratio obtained when the crystal is pumped by 500 mJ pulses. The time delay is the time duration after the pump beam hits the crystal. The photodiode signal shown in Fig. 4.1.1a can be fitted to an exponentially decaying curve with the decay time of 3.2 microseconds, which is the life time of the Ti^{3+} population in the upper laser level. Since the change of the amplification rate is canceled out by the P(r)/P ratio, the very fast lensing effect originates from the non-thermal part of the optically induced lensing. This signal as a function of time reveals both the average thermal lensing effect and the fast non-thermal

lensing effect. The signal before the pump pulse, indicated by the straight line, accounts for pure thermal lensing, while after the pump it is the summation of the thermal lensing and fast photoelastic lensing. As shown in Fig. 4.1.1b, when the pump energy is 500 mJ, right after the pumping where the lensing is strongest, the focal length is 5.65 m (by Eq. 3.3.2-3.3.4 in Ch.3.3), which includes all of the lensing effects. The steady state thermal lensing focal length is 7.75 m. For a lens system, the focal power can be expressed as

$$d = \frac{1}{f} = \sum_{i=1}^{n} \frac{1}{f_i} \qquad (4.1.1)$$

where f is the overall focal length and f_i is the focal length of each factor that contributes to the lensing effect. We can then calculate the non-thermal focal length to be 20.85 m which contributes 27% of the total lensing effect.

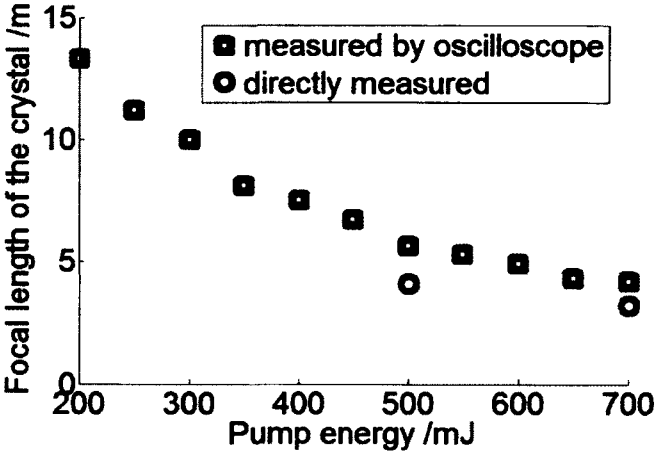

Figure 4.1.2 Comparison between the focal length of the crystal measured by oscilloscope and measured directly using an iris and a power meter

Figure 4.1.2 shows the focal length as a function of pump beam power. The square data points are obtained by the measurement discussed above (with the oscilloscope using the 80 MHz test beam), while the circle data points are taken with a pre-amplified 2 mJ, 30 Hz seed pulse, which is in phase with the pump. The latter has energy high enough to locate the focus by an iris and a power meter. The data obtained by this unique method are more reliable for the following reason: the profile of the pre-amplified beam is deteriorated by the amplifying process and it must have been focused already by the amplifier crystal with the same mechanism studied here.

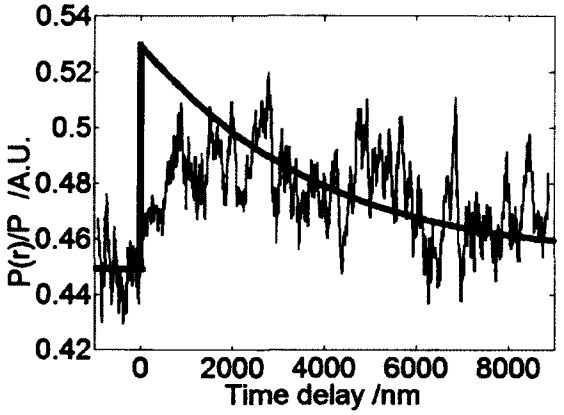

Figure 4.1.3 Signal when the pump energy is 700 mJ and test beam is P-polarized (the red line is the relaxation curve if not saturated)

Furthermore, the measurements show a population saturation effect when the pump energy approaches 700 mJ for P-polarized photons. Figure 4.1.3 does not show a clear relaxation. I explain it as the saturation of the upper level population, which restricts the gradient of refractive index change. In the laser

medium with absorption coefficient α, the power/energy absorbed at position z along the light path can be expressed as

$$A = P\frac{\alpha}{1-\exp(\alpha l)}\cdot\left[k\cdot\exp(-\alpha z)+(1-k)\exp(-\alpha(l-z))\right] \qquad (4.1.2)$$

where P is the total power/energy, and l is the total length of the light path which is *7 mm* in this case. In my setup, the pump beam is split into two parts to pump the crystal from both ends, one part with portion k of total power and the other part with portion *(1-k)*. k is 0.6 and α is 4.1 cm^{-1} here. The real pump beam profile is taken by a CCD camera (Fig. 4.1.4), when the pump energy is 500 mJ. Given the transverse distribution of the pump laser (Fig. 4.1.4), the distribution of absorption and thus the distribution of upper level population can be obtained (Fig. 4.1.5). The upper level population of some spots has already been close to the density of Ti^{3+} which is $8.6\times10^{25}m^{-3}$. Therefore, when the pump energy is further increased to 700 mJ, the saturation effect will be more significant.

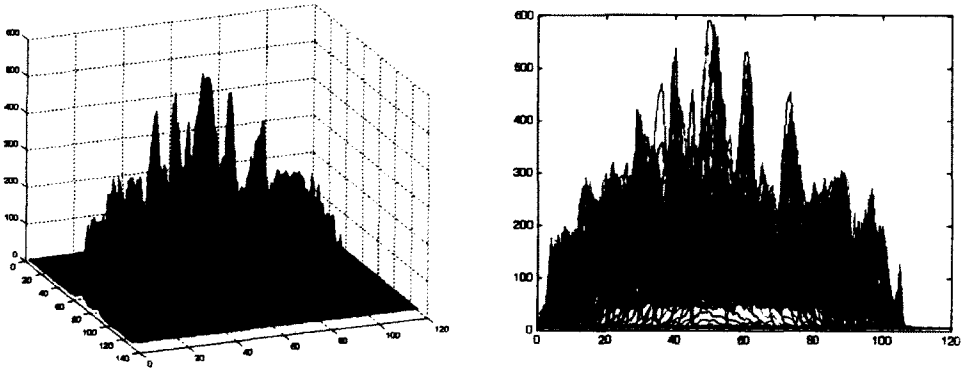

Figure 4.1.4 The pump beam profile taken by a CCD camera, QuantaRay PRO-290

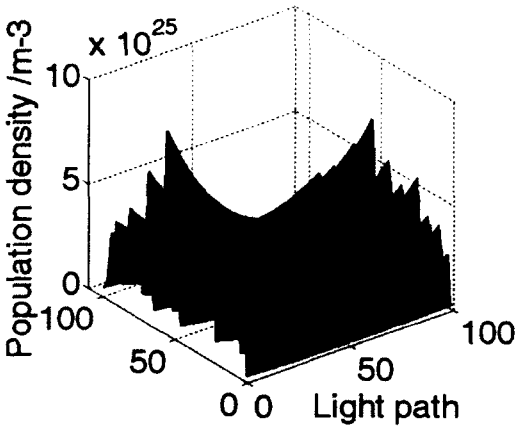

Figure 4.1.5 Population density in the sagittal plan of the crystal when pump energy is 500 mJ

4.2 Calculation of photoelastic constant for Ti:Sapphire crystal

The fast non-thermal lensing effect can be explained by a photoelastic model (Ch.2.5 and Ch.2.6). The basic mechanism for photoelastic lensing is that the excited ions have a larger volume so that they apply stress on the crystal lattice. As a result, the refractive index changes by the photoelastic effect. The photoelastic constants for Ti:Sapphire have not been measured yet. Researchers use the values for Cr:Sapphire crystal to do calculations for Ti:Sapphire. Here, the measurement results (Ch.4.1) are used to derive one of the photoelastic constants for the Ti:Sapphire crystal.

A 3-D model is built to simulate the population distribution in the crystal. For a flash light pumped high energy pulsed laser, the beam profile is far from a

Gaussian beam. Therefore, the model is based on the real beam profile taken by a CCD camera (Fig. 4.1.4). The calculated 3-D population distribution in the crystal by the real beam profile is shown in Fig. 4.1.5. In the model, I approximate the refractive index by a quadratic form, which is a radially varying index $n_r = n_0 - dn \cdot r^2$, where n_0 is the refractive index in the center. This assumption is also the base for the calculation of almost all lensing effects[121,83]. In this case the transmittance matrix is

$$M = \begin{bmatrix} \cos(l \cdot \sqrt{2dn / n_0}) & (\sqrt{2dn \cdot n_0})^{-1} \cdot \sin(l \cdot \sqrt{2dn / n_0}) \\ -\sqrt{2dn \cdot n_0} \cdot \sin(l \cdot \sqrt{2dn / n_0}) & \cos(l \cdot \sqrt{2dn / n_0}) \end{bmatrix}. \quad (4.2.1)$$

For a material with varying dn such as the crystal being measured here, the total transmittance matrix is the product of M for all small slices,

$$M = M_1 \cdots\cdots M_i \cdots\cdots M_m$$

$$= M_1 \cdots\cdots \begin{bmatrix} \cos(dl \cdot \sqrt{2dn_{x,y,i} / n_0}) & (\sqrt{2dn_{x,y,i} \cdot n_0})^{-1} \cdot \sin(dl \cdot \sqrt{2dn_{x,y,i} / n_0}) \\ -\sqrt{2dn_{x,y,i} \cdot n_0} \cdot \sin(dl \cdot \sqrt{2dn_{x,y,i} / n_0}) & \cos(dl \cdot \sqrt{2dn_{x,y,i} / n_0}) \end{bmatrix} \cdots\cdots M_m \quad (4.2.2)$$

where $dn_{x,y,i}$ is the dn of slice i. The radially varying index leads to a radial change in the optical pass deformation (OPD). The average focal length can be obtained by a quadratic fit for the change of the OPD with r,[102-104]

$$OPD(r) = OPD_0 - \frac{r^2}{2 \cdot f} \quad (4.2.3)$$

Here, the focal length f is known. The OPD can be calculated by $OPD(r) = \sum_{i=1}^{n} dl \bullet \frac{\Delta n_3}{N} N_{i,r}$ [88], where $\Delta n_3 / N$ is the change of index along the direction of the c-axis per population density, which is unknown in the relationship above. The task here is to derive $\Delta n_3 / N$ from the focal length and the population distribution which are known. Applying f = 20.86 m and the population distribution when the pump is 500 mJ (Fig. 4.1.5) to Equation 4.2.3, I fit the OPD by a quadratic polynomial (Fig. 4.2.1). I then take the average between sagittal and tangential plane, and finally get $\Delta n_3 / N = 0.8879 \mathring{A}^3$. Taking into account the error for the absorption coefficient, which is 20% provided by the manufacturer and the errors induced by the measurement, $\Delta n_3 / N = 0.9 \pm 0.3 \mathring{A}^3$ is a reasonable value with an error of 30%. It basically agrees with the value for Cr^{3+} doped sapphire crystal which is $1.3 \pm 0.1 \mathring{A}^3$. Applying the measurement and calculation results to the photoelastic law $\Delta n_3 = -\sum_{r=1}^{6} \frac{n^3}{2} p_{3r} s_r$ (Ch.2.6), where n=1.76, p is the strain-optic (elasto-optic) tensor and s is the strain with $s_1 = s_2 = 5.9 \pm 0.4 \mathring{A}^3 \bullet N$ and $s_3 = s_4 = s_5 = s_6 = 0$ (Ch.2.6), I can determine the photoelastic constant $p_{31} = -0.03 \pm 0.01$ for Ti:Sapphire crystal.

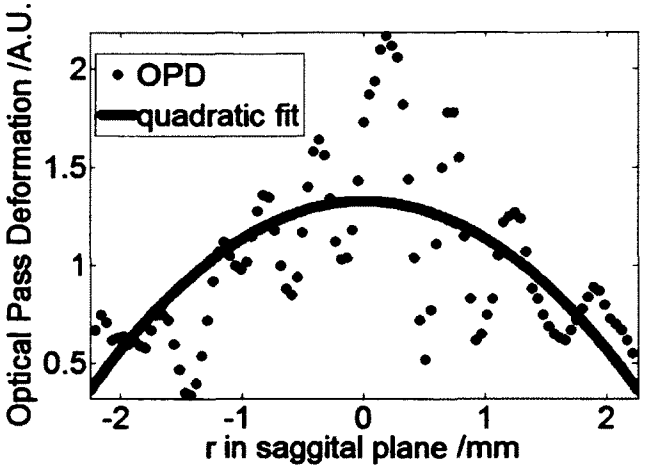

Fig.4.2.1 Radius dependent optical pass deformation (OPD) in sagittal plane and quadratic fit

This value is very useful for the design of Ti:Sapphire laser. To enhance the absorption coefficient and thus the gain of Ti:sapphire crystal, it is very common to cut the crystal with end facets at Brewster's angle. Sapphire is a hexagonal crystal favoring lasing with the electric field vector perpendicular to the C-axis. If the C-axis is aligned parallel to the Brewster facet transmission plane, the crystal works as a self cross-polarizer, which is very harmful to lasing. Furthermore, to grow the Ti:Sapphire crystal, the C-axis is naturally oriented perpendicular to the drawing axis, and the cylindrical laser rods are normally cut parallel to this axis to maximize yield. As a result, the Ti:Sapphire crystal is cut with their transmission plane electric field vector perpendicular to the C-axis in most cases (Fig. 4.2.2)[122]. The photoelastic constant determined in this study is the constant for such cutting, so it has general meaning.

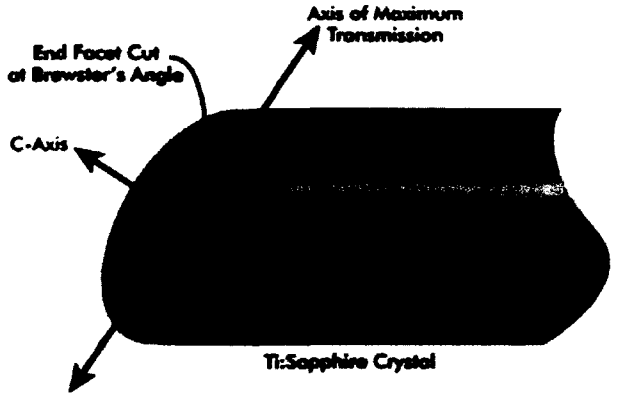

Fig.4.2.2 Brewster cut Ti:Sapphire crystal with electric field vector perpendicular to the C-axis[122]

In summary, the fast photoelastic lensing effect induced by the upper level population in a Ti:Sapphire crystal is measured by a unique setup. By analyzing the data, a photoelastic constant is determined, which is important for the design of Ti:Sapphire lasers. Given the focal length of the Ti:Sapphire crystal for the seed beam, the lensing effect can be easily compensated by curved mirrors. In the design of a multi-pass CPA system (Ch 3.1), I use a 5-pass configuration. One convex mirror with the focal length of -5 m is inserted after the first pass and another convex mirror with the focal length of -3 m is inserted after the third pass to compensate the lensing effect.

Chapter 5: Nonlinear Magneto Plasmonics

As a NLO effect sensitive to interface/surface, magnetic-induced second harmonic generation is a powerful method for probing the interface/surface magnetization (Ch.1.1.1). In this chapter, MSHG's interaction with another surface sensitive effect: surface plasmons (Ch.1.1.2), is studied. Since magneto-plasmonics describes hybrid systems where plasmonics and magnetic properties coexist, and MSHG is a nonlinear optical effect, the study here is called Nonlinear Magneto-Plasmonics.

In this study, a simplified sample system is proposed firstly because the overlap of the source of MSHG and SP makes the interaction between them more direct (Ch.1.1.3). Secondly, an enhanced MSHG signal is expected because of the field enhancement effect of SP (Ch.2.1). Most importantly, a more enhanced magnetic contrast (Ch.2.3) is also expected for NMP over MP systems. The magnetic contrast reveals a physical change induced by a magnetic field or different magnetization states, which plays an important role in MP systems. For example, in an active MP system, the modulation of surface plasmon wave vector can be expressed as a function of magnetic contrast[56]; in a new generation of bio-chemical sensing devices based on MP effect, the enhancement of sensitivity is a direct result of the reflection shift induced by the magnetic contrast[49,50,123]; and in more general cases, a high magnetic contrast is desirable for

magneto-optics (MO) device applications because of the better signal-to-noise ratio revealing strong coupling between light and magnetic property. In this study, I investigate the magnetic contrast in a NMP system.

5.1 Surface plasmon-enhanced transverse magnetic second harmonic generation

The transverse (T-) MSHG is first studied because of the following two reasons: 1) the surface plasmon-enhanced transverse magneto-optic Kerr effect is mainly studied[49-51,56-59], and therefore T-MSHG can give a direct comparison between MP and NMP; and 2) with a P-polarized fundamental incident beam, T-MSHG is also P-polarized (Eq.2.2.8), and therefore the P-polarized MSHG signal containing only T- component can be measured. The experimental setup is described in Chapter 3.2.

In previous research of MP, the common configuration is noble metal/ferromagnetic/noble metal heterostructure. Some complex structures or nano-structures were used in previous studies of MSHG interacting with SP. For example, Tessier et al. reported the reversal of MSHG contrast by SP generated from a standard Au/Co/Au heterostructure[58]. The enhanced MSHG signal by SP on nickel gratings has been observed by Newman et al.[124], and Valev et al.

showed that surface plasmon contributions to the MSHG signal can reveal the direction of the magnetization of Nickel nanostructures[125].

In this study, the single crystal iron film sample is critical because the crystal structure is the main source for the cubic magnetic anisotropy which results in the two-jump switching process (Ch.2.3). The two-jump process allows the separation of longitudinal and transverse magnetic contrast. The 10-nm thick Fe film samples are grown by molecular beam epitaxy at room temperature on <100> MgO substrates. The substrates are cleaned with isopropyl alcohol and annealed *in-situ* to 823 K for 5 minutes prior to growth. Reflection high energy electron diffraction (RHEED) measurements indicate single-crystal Fe growth[36].

5.1.1 Surface plasmon-enhanced transverse MSHG and contrast ratio

Sample I is a 10-nm thick single crystal Fe film grown on a MgO substrate described above with axis [110] along the x-direction (Fig. 5.1.1), capped with a 40-nm thick Au layer. This structure is expected to have a huge field enhancement due to the Au cap layer. A very large MSHG signal is generated under ATR condition because of the enhancement of the fundamental field (Fig. 5.1.2 (a)). The magnetic contrast in the MSHG signal is negligible when a magnetic field of H =+/- 100 Oe is applied along the y-direction. This result provides some important information: First, the experiment confirms that the

enhanced MSHG signal under ATR condition is generated at the Au surface (Au/air interface)[44,52], and not the Fe/Au interface because there is no magnetic response. Second, it shows that the MSHG response from the Fe-MgO interface is negligible under this configuration.

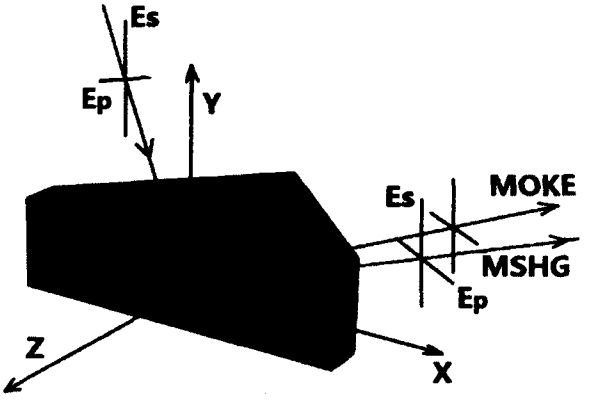

Figure 5.1.1 Coordinate system of the experimental setup

Of more interest is Sample II, which is a 10-nm thick single-crystal Fe film grown on a MgO substrate with axis [110] along the x direction. This structure is expected to exhibit large SP-enhanced magnetic response from the Fe surface (Fe/air interface). One common concern is that the Fe film is not suitable for huge field enhancement due to its large damping of electromagnetic fields compared to noble metals like Ag and Au. Actually, Fe films have been widely studied in surface plasmon coupled emission (SPCE), plasmon coupled chemi-luminescence, and long-range surface polaritons (LRSPs) by the ATR method[126-128].

Figure 5.1.2 (b) shows the angle-of-incidence dependent T-MSHG signal from sample II for applied magnetic fields H =+/- 100 Oe. Note that the ATR curve is not as sharp as that of sample I (Fig. 5.1.2 (a)) as it is stretched out due to absorption, i.e. strong damping. Without ATR (θ < 40°, where θ is the incident angle, as defined in Fig. 3.2.3), the MSHG signal is very small and the magnetic contrast is negligible. Under ATR condition, both the MSHG signal strength and the contrast ratio become enhanced by the SP field. As a result, a very strong signal with good magnetic contrast is observed. This is the SP-enhanced T-MSHG effect.

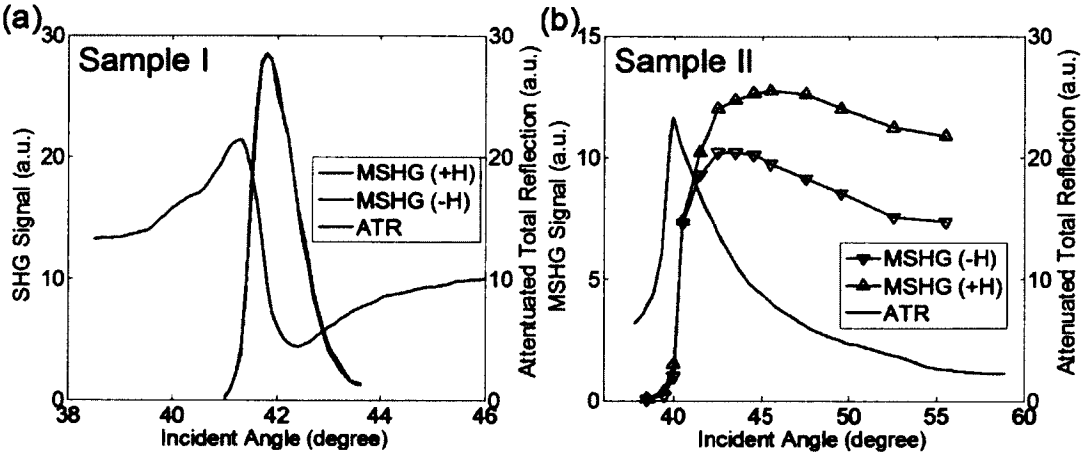

Figure 5.1.2 (a) MSHG signal from sample I with large SP enhancement but no apparent magnetic contrast; (b) Sample II with large SP enhancement and huge magnetic contrast

A comparison between T-MSHG under ATR configuration and normal reflection configuration is shown in Figure 5.1.3. The incident angle is 44° for ATR

configuration, and 45° for reflection configuration. The data show a strong enhancement of the signal strength and contrast ratio of MSHG by SP.

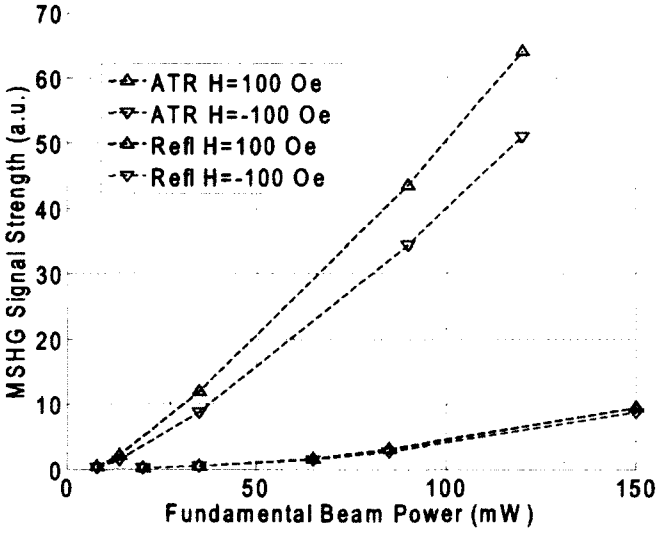

Figure 5.1.3 MSHG signal strength under ATR configuration (SP enhanced) and under normal reflection configuration from sample II

The hysteresis loops for SP-enhanced T-MSHG and T-MOKE and the contrast ratios based on the hysteresis loops are shown in Figure 5.1.4. Both show an increased contrast ratio as the total reflection becomes more attenuated. However, the contrast ratio of T-MSHG is more than one order of magnitude larger than for T-MOKE. The combination of large magnetic contrast, strongly enhanced T-MSHG and high surface sensitivity shows great potential for a new generation of nonlinear magneto-optical SP sensors for bio-chemical applications.

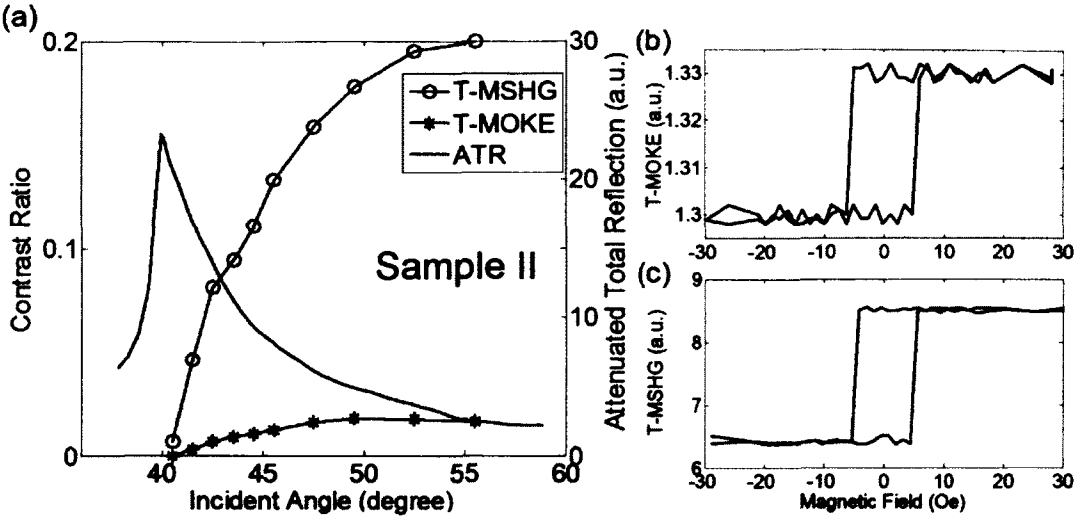

Figure 5.1.4 (a) Contrast ratio of T-MSHG and T-MOKE under ATR condition; (b) and (c) hysteresis loops obtained when the incident angle is 45.6° for P-polarized light-in and P-polarized light-out configuration. T-MSHG has much larger contrast ratio than T-MOKE

5.1.2 Discussion

The SP-enhanced SHG originates from the metal/air interface[37,52-54]. Here, the iron side of the iron/air interface is the source of MSHG under ATR condition. Simon et al. show that under ATR condition, SHG at the metal/air interface is much greater than that at the substrate/metal interface[52], and Tsang points out that the interference between the two contributions makes up the noise-like background in the vicinity of ATR[53]. In our measurement (Fig. 5.1.2(b)), the SHG signal without ATR is very small, so that SHG at the substrate/metal interface is not considered in our simulation. According to the surface-plasmon field-enhancement theory, the value of the field enhancement is given by the

ratio of the field intensity (light intensity) on the metal surface (the metal/air interface) divided by the incoming field intensity in the prism (substrate/metal interface)[37]. Hence, the enhancement of SHG can be defined as the square of the field enhancement. Since only the relative intensity and trends of SHG are simulated here, the propagation of the SHG beam is not being considered in the model. In the simulation, the refractive index of the prism is 1.5, the refractive index of MgO is 1.73 and ε_{iron}= -4.5+22i[129]. This model agrees with our experimental data (Fig. 5.1.2(a)) from sample I very well (Fig. 5.1.5(a)), because the SHG signal comes from the metal/air surface and it is a non-magnetic process in this case. However, when taking into account the magnetic contribution, it becomes more complex and there is a big difference between experimental T-MSHG data for sample II (Fig. 5.1.2(b)) and the simulated SHG values (Fig. 5.1.5(b)), although the experimental and simulated ATR curves are almost identical. The experimental SHG data stretch out and keep a high intensity as the incident angle increases, while the calculated SHG intensity drops very fast. Here the trends of field intensity in each direction (x and z in Fig.5.1.1) need to be considered.

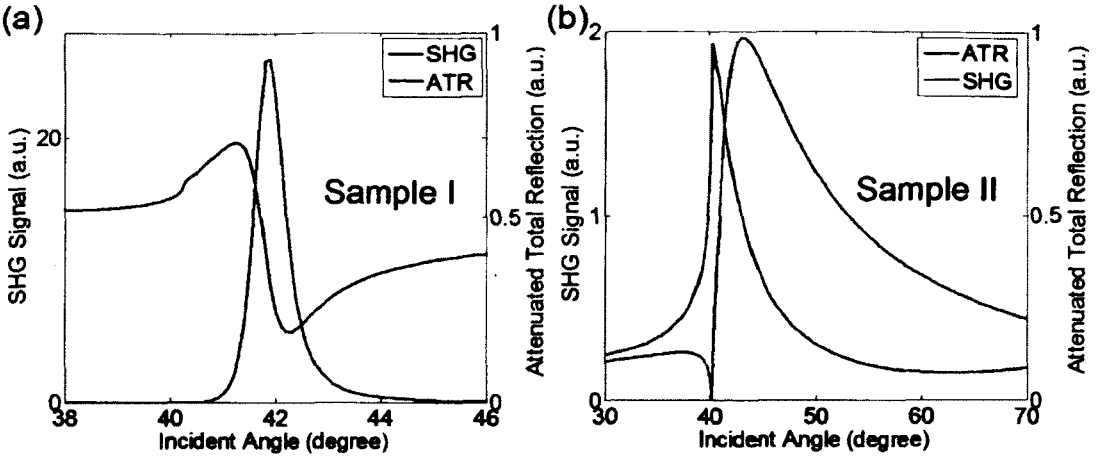

Figure 5.1.5 Simulated ATR and SHG for sample I (a) and II (b)

The strength of the incident P-polarized light at the prism/iron interface can be decomposed into two components: $Ez_0 = E_0 \sin \theta'$ and $Ex_0 = E_0 \cos \theta'$, where θ' is the incident angle at that interface. After the SP field-enhancement factor is also considered, Ez and Ex at the iron/air interface can be calculated and are displayed in Figure 5.1.6(a), showing different trends as the incident angle increases. The second-order surface susceptibility tensor components in the x-direction (χ_{xxx} , χ_{xzx} and χ_{xzz}) contribute most to the second-harmonic generation[52,54] because the generation of a surface wave at the SHG frequency is a surface specific process. As a result, the intensity of T-MSHG can be simplified as:

$$I^{T-MSHG}(+M) = \varepsilon_0^2 \cdot \left(\chi_{xxx}^{odd} \cdot E_x^2 + \chi_{xzz}^{odd} \cdot E_z^2 + \chi_{xzx}^{even} \cdot 2E_z E_x\right)^2 \qquad (5.1.1)$$

and $$I^{T-MSHG}(-M) = \varepsilon_0^2 \cdot \left(-\chi_{xxx}^{odd} \cdot E_x^2 - \chi_{xzz}^{odd} \cdot E_z^2 + \chi_{xzx}^{even} \cdot 2E_z E_x\right)^2, \qquad (5.1.2)$$

depending on the direction of M. From this expression, I notice that the trend of T-MSHG intensity as a function of incident angle will be affected largely by the weight of E_x^2 and E_z^2. In other words, knowing the trends of E_x and E_z as a function of incident angle (Fig. 5.1.5(a)), we can calculate the intensity of T-MSHG, if we know the relative value of χ_{xxx}^{odd} and χ_{xzz}^{odd}.

I found that if χ_{xxx}^{odd} dominates, the T-MSHG intensity exhibits a very steep drop with increasing angle-of-incidence (Fig. 5.1.5(b), Set 2), while if χ_{xzz}^{odd} dominates, T-MSHG remains a high value for large incident angles (Fig. 5.1.5(b) set 1). The latter one agrees with our experimental data (Fig. 5.1.2(b)) very well. Hence, there exists a great anisotropy in the second-order susceptibility tensor of T-MSHG, and for the single-crystal iron film surface, χ_{xzz}^{odd} dominates the nonlinear susceptibility tensor. In this case, the expression of transverse MSHG can be simplified as

$$I^{T-MSHG}(\pm M) = \varepsilon_0^2 \cdot \left(\pm \chi_{xzz}^{odd} \cdot E_z^2 + \chi_{xzx}^{even} \cdot 2E_z E_x\right)^2. \qquad (5.1.3)$$

I note that there is oxide layer inevitably on the top of the iron film. This is favorable for the SHG due to the Bloembergen effect[2]. However, the oxide layer only has very tiny effect on the SP according to the simulation. Further more, since the MSHG signal has been measured under ATR and reflection

configuration with the sample, the new effects discussed in this study have nothing to do with the oxide layer.

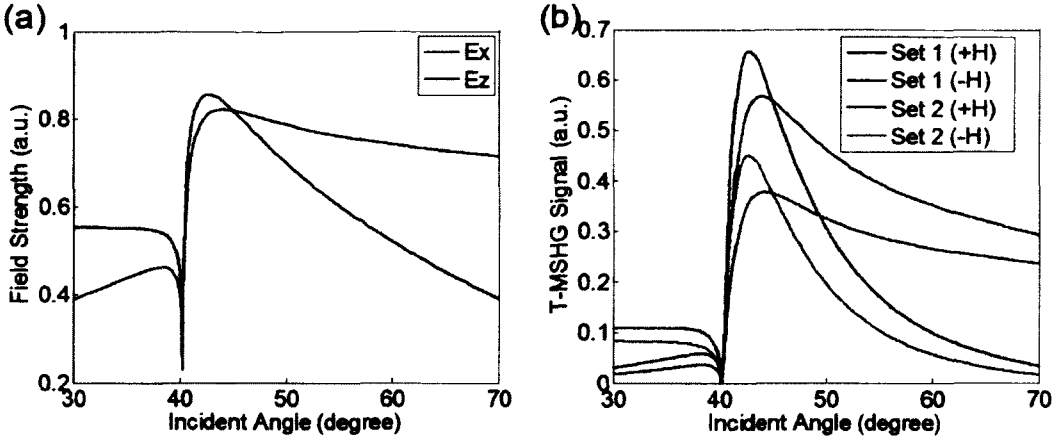

Figure 5.1.6 (a) Field strength of Ex and Ez , (b) Simulated T-MSHG signal. Set 1: $\chi_{xxx}^{odd} / \chi_{xzz}^{odd} = 1:100$, *Set 2:* $\chi_{xxx}^{odd} / \chi_{xzz}^{odd} = 100:1$

5.2 Magnetic contrast tuning effect

In order to elucidate the origin of the SP-enhanced contrast ratio in NMP system, the longitudinal (L-) MSHG is also studied. For a P-polarized fundamental field, the T-MSHG is P-polarized (Ch.2.2, Eq.2.2.8), while the L-MSHG contains both P and S component. The T-MSHG can be filtered out by a S-polarized analyzer. However, for pure S-polarized MSHG signal, there are only odd nonlinear magnetic tensor components, as a result the contrast ratio $C = 0$ because $(+\chi^{odd})^2 = (-\chi^{odd})^2$ and $I^{2\omega}(+M) = I^{2\omega}(-M)$,. The common practice is to offset the polarizer a few degrees to induce some background as $(A+\chi^{odd})^2 \neq (A-\chi^{odd})^2$,

which is call S*-polarized[15,93]. As a result, the L-MSHG data will be mixed with some T-MSHG component.

5.2.1 The change of hysteresis loops and the tuning of contrast ratio

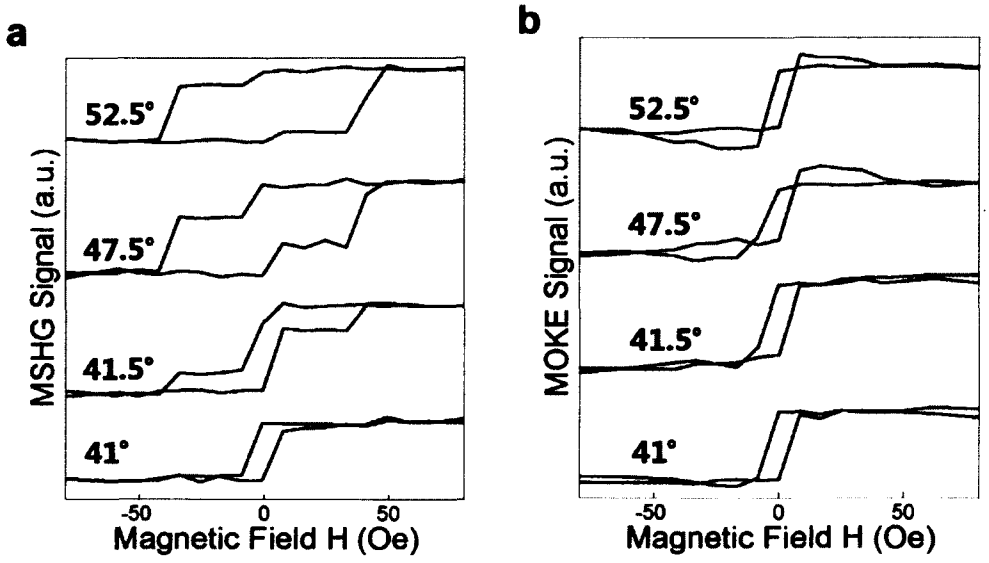

Figure 5.2.1 (a) MSHG and (b) MOKE hysteresis loops under ATR configuration with different incident angle

Figure 5.2.1 (a) shows MSHG hysteresis loops taken at different incident angles, θ = 41°, 41.5°, 47.5°, and 52.5°, and the analyzer is set to be 10° offset from the S polarization. There is hardly any magnetic contrast at the angle of total reflection (θ = 40°), the same as for T-MSHG (Fig. 5.1.4(a)). For θ = 41°, ATR just begins, and the hysteresis loop shows clear contrast with only the L-component switching at H = 5 Oe. The switching of T-component at H = 40 Oe begins to appear at θ = 41.5°, but the L-component still dominates the switching. With increasing incident angle (θ = 47.5°), the T-component becomes more enhanced,

and eventually at θ = 52.5°, where the reflection is very small and close to the bottom of the ATR curve, the T-component dominates the hysteresis loop. For comparison, Figure 5.2.1(b) shows hysteresis loops for SP-enhanced MOKE. At θ = 41° and 41.5°, the T-component is negligible. At larger angles, θ = 47.5° and θ = 52.5°, the T-component becomes enhanced but remains at a relatively low level as compared to the L-component. This important observation demonstrates the large tuning effect of L- and T-component in MSHG which is absent in MOKE. There is no such huge effect for MSHG under normal reflection geometry or MSHG under Kretschmann-Raether configuration with S-polarized fundamental field.

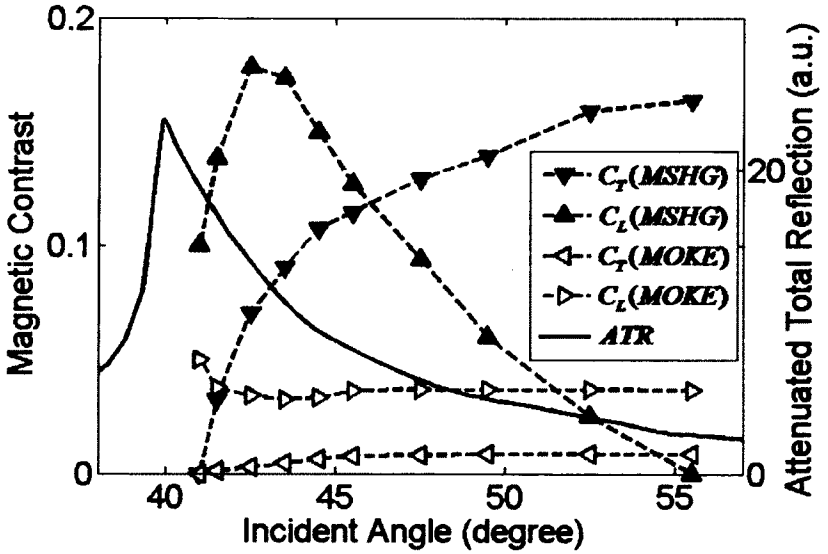

Figure 5.2.2 Magnetic contrast of MSHG and MOKE under ATR

Figure 5.2.2 shows the magnetic contrast of MSHG and MOKE as a function of the incident angle, together with the ATR curve. The most important finding is

that for L- and T- MSHG, the contrast ratios C_L (—▲—) and C_T (—▼—) (refer to Ch.2.3) can be tuned by the SP resonance with opposite trends. I call this magnetic contrast tuning with nonlinear magneto-plasmonics. C_L initially increases sharply when ATR begins and reaches its maximum at around 42.5°, but then decreases as θ increases further, until it totally disappears at around 55°. In contrast, C_T increases slowly and steadily over the whole range. This trend is independent of the setting of analyzer. Note that the same tuning effect and trend of C_L and C_T are obtained when the external magnetic field is aligned along the transverse direction, i.e. along axis [110]. This proves that the tuning effect is directly related to the direction of magnetization, rather than the external magnetic field.

5.2.2 Discussion

To elucidate the origin of the large tuning effect in the MSHG contrast ratios, C_T and C_L are studied as a function of the angular position α of the analyzer[11,14] (α = 0 corresponds to p-polarization). According to the analysis of the magnetic contrasts for a two-jump system in Ch.2.3, magnetic contrasts for L- and T-MSHG can be expressed as:

$$C_L = 2\frac{k_L \tan(\alpha)\cos(\varphi_L)}{1+k_T^2+k_L^2\tan^2(\alpha)} \quad \text{and} \quad C_T = 2\frac{k_T \cos(\varphi_T)}{1+k_T^2+k_L^2\tan^2(\alpha)} \qquad (5.2.1)$$

where k_T and k_L are the ratios of magnitude between the magnetic and non-magnetic MSHG response for T- and L-magnetization components, both of

which are composed of fundamental fields and corresponding effective susceptibility tensors. ϕ_T and ϕ_L are the phase differences between the magnetic and non-magnetic MSHG response for T- and L-magnetization components, respectively. Note that when $k_T = 0$, the expression for C_L becomes identical to the one for the one-jump MSHG hysteresis loop measured in the L-geometry[58,94]. Furthermore, k_T and ϕ_T can only be obtained from the two-jump MSHG hysteresis loop, because Eq.5.2.1 becomes meaningless without k_L and α. With the measured values of the contrast ratios as a function of analyzer angle, k and ϕ can be obtained by fitting the contrast ratios to Eq.5.2.1.

Figures 5.2.3(a) and (b) show the ratios of magnitude and phase differences as a function of incident angle under ATR condition for T- and L-magnetization components, respectively. The ratios k_T and k_L hardly change within experimental errors and hence cannot account for the large tuning effect. In contrast, ϕ_L exhibits a large monotonic increase from 72° to 90° over the ATR range, while ϕ_T decreases from 88° to 77°. This trend is consistent with the large decrease of C_L and the steady increase of C_T with increasing incident angle under ATR. Therefore, the magnetic contrast tuning effect originates from the change of relative phases caused by SP. The phase difference between magnetic and non-magnetic components of MSHG signal is known to be related to the relative orientation of magnetization and the wave vector of fundamental fields[7,15,16].

Since the L- and T- magnetization components are normal to each other, C_T and C_L display opposite trends.

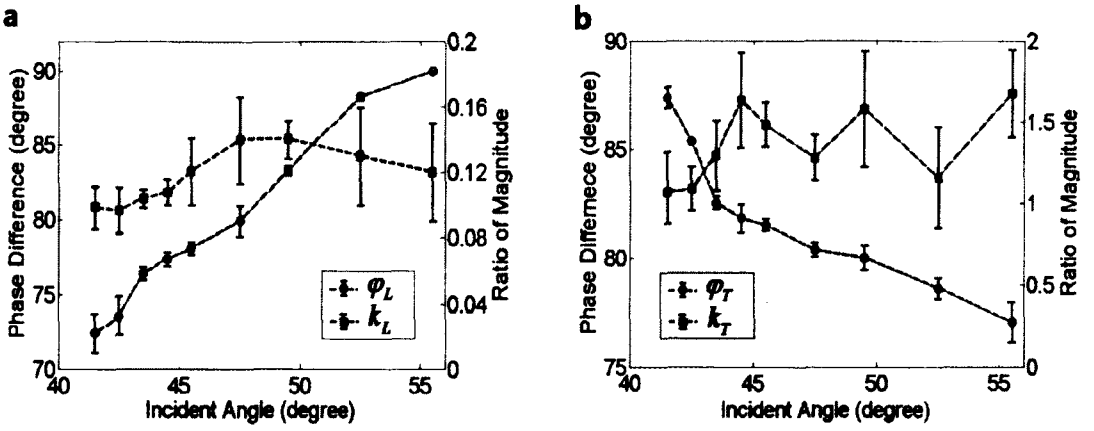

Figure 5.2.3 Phase difference and ratio of magnitude as a function of incident angle. (a) L-MSHG, (b) T-MSHG.

In summary, magnetic contrast tuning in single-crystalline iron film with nonlinear magneto-plasmonics has been demonstrated. Such a system opens the way for simultaneously investigating both longitudinal and transverse magnetization components regardless of the external magnetic field. By studying MSHG hysteresis loops as a function of incident angle and polarization angle, and by fitting the magnetic contrasts to theoretical formulas, I find that the tuning effect originates from the change of relative phase between magnetic and non-magnetic MSHG components caused by surface plasmons.

5.3 Conclusion

In this study, I first demonstrated that a single-crystal ferromagnetic Fe film allows a detailed study of NMP, because MSHG and SP are both surface

sensitive effects. This is of interest to the development of MP devices. By studying the SP enhancement effect on transverse MSHG, I demonstrated that the contrast ratio of SP-enhanced transverse MSHG is more than one order of magnitude larger than the SP-enhanced transverse MOKE, which shows great advantage of NMP over MP for sensor applications. Furthermore, a method to study pure surface magnetization is provided. The experimental results also suggest a strong anisotropy exists among the second-harmonic generation susceptibility tensors. By studying the hysteresis loops of SP-enhanced MSHG with different incident angle and different analyzer polarization, a contrast ratio tuning effect is discovered, an important finding in this dissertation. This study demonstrates that the longitudinal and transverse MSHG are governed by the direction of magnetization, rather than the external magnetic field. With the enhancement effect, both L- and T- MSHG can be studied simultaneously for a material with cubic magnetic anisotropy. This new effect enhances the sensing of magnetic switching, which has potential usage in quaternary magnetic storage systems because it enables the read-out of all four magnetization states from crystalline iron with high contrast ratio, and it is also of interest for bio-chemical sensor applications due to its very high surface sensitivity and simple structure.

Chapter 6: Conclusion

Two NLO effects are studied in this dissertation. The magnetic-induced second harmonic generation (MSHG) interacting with surface plasmon, called "nonlinear magneto-plasmonics" (NMP), and the nonlinear index induced by a strong pump beam in Titanium doped sapphire crystal, which is called population-induced nonlinear index effect.

In the study of population-induced nonlinear index effect, a fast measuring method is developed to catch the fast lensing effect in the scale of several microseconds. The photoelastic constant obtained is very useful for the design of high power Ti:Sapphire lasers and amplifiers. A spatially and temporally homogenized chirped pulse amplifier, whose performance is better than the available commercial ones, is built during this study.

The study of nonlinear magneto plasmonics is significant and the results will be of immediate interest to the large community working in this area. The terminology NMP is created by our group. Magnetic contrast tuning in single-crystalline iron film and the enhancement of MSHG signal with nonlinear magneto-plasmonics are demonstrated. The two-jump switching process is studied systematically for the first time. Such a system opens the way for simultaneously investigating longitudinal and transverse magnetization

components regardless of the external magnetic field. By studying MSHG hysteresis loops as a function of incident angle and polarization angle, and by fitting the magnetic contrasts to theoretical formulas, I find that the tuning effect in longitudinal and transverse magnetic contrasts originates from the change of relative phase between magnetic and non-magnetic MSHG components caused by surface plasmon. This new effect has potential usage in quaternary magnetic storage systems, and it is also of interest for bio-chemical sensor applications due to its very high surface sensitivity and simple structure.

BIBLIOGRAPHY

1. Y. R. Shen, *The Principles of Nonlinear Optics* (Wiley, 1984)

2. N. Bloembergen, *Nonlinear Optics* (World scientific, 1981).

3. R. W. Boyd, *Nonlinear Optics* (Benjamin: New York,1965)

4. P. Franken, A. Hill, C. Peters, and G. Weinreich. "Generation of Optical Harmonics". *Physical Review Letters* 7 (4): 118. 1961

5. W. G. Rado, The nonlinear third order dielectric susceptibility coefficients of gases and optical third harmonic generation, *Applied Physics Letters* (Volume:11 , Issue: 4) 123 - 125, 1967

6. D. A. Kleinman, Theory of optical parametric noise, *Phys. Rev.* 174 (3), 1027, 1968

7. R. H. Stolen and A. Ashkin, Optical Kerr effect in glass waveguide, *Appl. Phys. Lett.* 22, 294 (1973)

8. K. H. Bennemann, *Nonlinear Optics in Metals*, ClarendonPress: Oxford, 1998.

9. N. Bloembergen and P. S. Pershan, Light waves at the boundary of nonlinear media. *Physical Review*, **128**, 606–622, 1962

10. A. Kirilyuk and T. Rasing, "*Magnetization-induced second harmonic generation*," in *Handbook of Magnetism and Advanced Magnetic Materials*. (John Wiley & Sons, Ltd. 2007, Volume 3: Novel Techniques for Characterizing and Preparing Samples).

11. J. Reif, J. C. Zink, C. M. Schneider, and J. Kirschner, Effects of surface magnetism on optical second harmonic generation. *Physical Review Letters*, **67**, 2878–2881, 1991.

12. J. Reif, C. Rau, and E. Matthias. Influence of magnetism on second harmonic generation. *Physical Review Letters*, **71**, 1931–1934, 1993.

13. A. Kirilyuk, Nonlinear optics in application to magnetic surfaces and thin films, *J. Phys. D: Appl. Phys.* 35, R189 - R207, 2002.

14. R. Atkinson and N. F. Kubrakov, Boundary conditions in the simplest model of linear and second harmonic magneto-optical effects. *Physical Review B*, 65, 014432, 2002.

15. H. B. Zhao, D, Talbayev,G. Lüpke *et al.* Interface Magnetization Reversal and Anisotropy in Fe/AlGaAs(001). *Phys.Rev.Lett.* 95,137202 ,2005.

16. H. A. Wierenga, W. de Jong, M. W. J. Prins, *et al.* Interface magnetism and possible quantum well oscillations in ultrathin Co/Cu films observed by magnetization induced second harmonic generation. *Physical Review Letters*, **74**, 1462–1465, 1995.

17. H. A. Wierenga, M. W. J. Prins, D. L. Abraham, and Th. Rasing, Magnetisatization-induced optical second-harmonic generation: a probe for interface magnetism. *Physical Review B*, **50**, 1282–1285,1994.

18. H. A. Wierenga, M. W. J. Prins, and Th. Rasing, Magnetisatization-induced optical second-harmonic generation from magnetic multilayers. *Physica B*, **204**, 281–286, 1995.

19. R. Vollmer, A. Kirilyuk, H. Schwabe, *et al.* Direct comparison of nonlinear and linear Kerr effect measurements on thin Co films on Cu(001). *Journal of Magnetism and Magnetic Materials*, **148**, 295–297, 1995.

20. R. Vollmer, M. Straub, and J. Kirschner, Second harmonic generation from the Cu(001) surface. *Surface Science*, **352**, 684–688, 1996.

21. R. Vollmer, M. Straub, and J. Kirschner, Nonlinear magneto-optical Kerr measurements on Fe(110). *Surface Science*, **352**, 937–941, 1996.

22. M. Straub, R. Vollmer, and J. Kirschner, Surface magnetism of ultrathin γ -Fe films investigated by nonlinear magneto-optical Kerr effect. *Physical Review Letters*, **77**, 743–746, 1996.

23. Q. Y. Jin, H. Regensburger,R. Vollmer and J. Kirschner, Periodic oscillations of the surface magnetization during the growth of Co films on Cu(001). *Physical Review Letters*, **80**, 4056–4059, 1998.

24. K. J. Veenstra, P. E. Hansen, A. Kirilyuk, *et al.* Surface magnetism of Ni(110) probed by magnetic second harmonic generation. *Journal of Magnetism and Magnetic Materials*, **198–199**, 695–697, 1999.

25. K. J. Veenstra, A. V. Petukhov, A. P. de Boer, And Th. Rasing, Phase-sensitive detection technique for surface nonlinear optics. *Physical Review B*, **58**, R16020–R16023, 1998.

26. K. J. Veenstra, A. V. Petukhov, E. Jurdik, and Th. Rasing, Strong surface state effects in nonlinear magneto-optical response of Ni(110). *Physical Review Letters*, **84**, 2002–2005, 2000.

27. A. Kirilyuk, Th. Rasing, M. A. M. Haast, and J. C. Lodder, Probing structure and magnetism of CoNi/Pt interfaces by nonlinear magneto-optics. *Applied Physics Letters*, **72**, 2331–2333, 1998.

28. L. C. Sampaio, J. Hamrle, A. Mougin, *et al.* In-depth selectivity of the magnetic second-harmonic generation of light in a multilayer structure. *Physical Review B*, **70**, 104403, 2004.

29. M. Fiebig, D. Fr¨ohlich, B. B. Krichevtsov, and R. V. Pisarev, R.V. Second harmonic generation and magnetic-dipoleelectric-dipole interference in antiferromagnetic Cr2O3. *Phys. Rev. Lett.* 73, 2127–2130, 1994.

30. M. Fiebig, D. Fr¨ohlich, G. Sluyterman, and R. V. Pisarev, Domain topography of antiferromagnetic Cr2O3 by 2nd-harmonic generation. Applied Physics Letters, 66, 2906–2908, 1995.

31. L. C. Sampaio, J. Hamrle, V. V. Pavlov, *et al.* Magnetization-induced second-harmonic generation of light by exchangecoupled magnetic layers. *Journal of the Optical Society of America B*, **22**, 119–127, 2005.

32. L. C. Sampaio, A. Mougin, J. Ferr´e, J., *et al.* Probing interface magnetism in the FeMn/NiFe exchange bias system using magnetic second harmonic generation. *Europhysics Letters*, **63**, 819–825, 2003.

33. V. K. Valev, M. Gruyters, A. Kirilyuk, And Th. Rasing, Direct observation of exchange bias related uncompensated spins at the CoO/Cu interface. *Physical Review Letters*, **96**, 067206, 2006.

34. V. K. Valev, M. Gruyters, A. Kirilyuk, and Th. Rasing, Temperature dependence of magnetization-induced second harmonic generation at buried exchange-biased interfaces. *Physical Review B*, **73**, 233101, 2006.

35. V. K. Valev, F. Dalla Longa, J. T. Kohlhepp, et al. Observation of periodic oscillations in magnetization-induced second harmonic generation at the Mn/Co interface. Physical Review B, 75, 012401, 2007.

36. Y. Fan, K. J. Smith, G. Lüpke, A. T. Hanbicki, B. T. Jonker, *et al.* Exchange bias of the interface spin system at the Fe/MgO interface. *Nature Nanotechnology 10*,1038-1043, 2013.

37. H. Raether, Surface Plasmons on Smooth and Rough Surfaces and on Gratings. (Springer Tracts in Modern Physics, 1988).

38. V.M. Agranovich, and D.L. Mills, *Surface Polaritons* (North Holland, Amsterdam1982)

39. R.H. Ritchie, Plasma Losses by Fast Electrons in Thin Films, *Phys. Rev.* 106, 874, 1957

40. H. Raether, *Physics of Thin Films* (Academic New York, 1977)

41. A.D. Boardman, *Electromagnetic Surface Modes* (Wiley, New York 1982)

42. H. Raether, Roughness on Silver films, *Surface Science* 140, 31 (1984)

43. G. Hincelin, Enhancement of surface and volume photoeffects in cesiated Al thin films by controlled excitation of surface plasma waves at low photon energies, *Phys. Rev. B* 24, 787–805 (1981)

44. W. H. Weber and G. W. Ford, Optical electric-field enhancement at a metal surface arising from surface-plasmon excitation, *Optics Letters*, Vol. 6, Issue 3, pp. 122-124 (1981)

45. F. Wang, M. Wang, D. Li, and D. Yang, 1Localized surface plasmon resonance enhanced photoluminescence from SiNx with different N/Si ratios, *OPTICAL MATERIALS EXPRESS*, Vol. 2, No. 10, 1437-1448 (2012)

46. Z. Utegulov, B. T. Draine, *et al, Surface-plasmon enhancement of Brillouin light scattering from gold-nanodisk arrays on glass,* SPIE Optics and Photonics, Vol, 6641,66411M-1 - 66411M-10 (2007)

47. S. Nie, and S. R. Emory, Probing Single Molecules and Single Nanoparticles by Surface-Enhanced Raman Scattering. *Science* **275**(5303): 1102–6. doi:10.1126/science.275.5303.1102 (1997)

48. S.L. McCarthy, S.L. ,and J. Lambe, Enhancement of light emission from metal - insulator - metal tunnel junctions, *Applied Physics Letters,* Volume:30 , Issue: 8 (1977)

49. B. Sepúlveda, A. Calle, L. M. Lechuga, and G. Armelles, Highly sensitive detection of biomolecules with the magneto-optic surface-plasmon-resonance sensor, *Opt. Lett.* **31**(8), 1085–1087 (2006)

50. D. Regatos, D. Fariña, A. Calle, A. Cebollada, B. Sepúlveda, G. Armelles, and L. M. Lechuga, Au/Fe/Au multilayer transducers for magneto-optic surface plasmon resonance sensing, *J. Appl. Phys.* 108, 054502 (2010)

51. J. Pistora, M. Lesnak, O. Vlasin, *et al.* Surface plasmon resonance sensor with Magneto-Optical thin film. *Acta Electrotechnica et Informatica,* Vol. 10, No. 3, 19–21 (2010)

52. H. J. Simon, D. E. Mitchell, and J. G. Watson, Optical second-harmonic generation with surface plasmons in silver films, *Phys. Rev. Lett.* **33**(26),1531-1534 (1974)

53. T. Y. F. Tsang, Surface-plasmon-enhanced third-harmonic generation in thin silver films, *Opt. Lett.* **21**(4), 245–247 (1996)

54. S. Palomba and L. Novotny, Nonlinear excitation of surface plasmon polaritons by four-wave mixing, *Phys. Rev. Lett.* **101**, 056802 (2008)

55. V.V. Temnov, G. Armelles, U. Woggon, *et al.* Active magneto-plasmonics in hybrid metal–ferromagnet structures. *Nature Photon.* 4, 107–110 (2010)

56. V.V. Temnov, Ultrafast acousto-magneto-plasmonics. *Nature Photon. 6*, 728–736 (2012)

57. V.K. Valev, *et al.* Plasmons reveal the direction of magnetization in nickel nanostructures. *ACS Nano* 5, 91–96 (2011)

58. G. Tessier, C. Malouin, P. Georges, *et al.* Magnetization-induced second-harmonic generation enhanced by surface plasmons in ultrathin Au/Co/Au metallic films. *Appl. Phys. B* 68, 545–548 (1999)

59. V.I. Safarov, V.A. Kosobukin, C. Hermann, et al. Magneto-optical effects enhanced by surface plasmons in metallic multilayer films. *Phys. Rev. Lett.* 73,3584-3587(1994)

60. P. Weinberger, John Kerr and his Effects Found in 1877 and 1878. *Philosophical Magazine Letters* **88** (12): 897–907(2008)

61. R. H. Stolen and A. Ashkin, Optical Kerr effect in glass waveguide, *Appl. Phys. Lett.* 22, 294 (1973)

62. http://en.wikipedia.org/wiki/Pockels_effect

63. http://en.wikipedia.org/wiki/Photoelastic_effect

64. J.W. Dally, and W.F. Riley, *Experimental Stress Analysis,* 3rd edition, (McGraw-Hill Inc., 1991)

65. J.H. Wray, J.T. Neu, Refractive index of several glasses as a function of wavelength and temperature, *J. Opt. Soc. Am.*, 59(6), 774-776 (1969)

66. J. Matsuoka, N. Kitamura, S. Fujinaga, T. Kitaoka, H. Yamashita, Temperature dependence of refractive index of SiO2 glass, *J. Non-Crystalline Solids*, 135, 86-89 (1991)

67. B. J. Frey, D. B. Leviton, Automation, operation, and data analysis in the cryogenic, high accuracy, refraction measuring system (CHARMS), SPIE 5904, 212-221 (2005)

68. W. Koechner, *Solid-State Laser Engineering*, 6th edn., (Springer, Berlin, 2006)

69. B. Bendow and P. D. Gianino, Optics of thermal lensing in solids, *Appl. Opt.* 12 (4), 710 (1973)

70. V. Magni, Multielement stable resonators containing a variable lens, *J. Opt. Soc. Am.* A 4 (10), 1962 (1987)

71. D. Metcalf *et al.*, Laser resonators containing self-focusing elements, *Appl. Opt.* 26 (21), 4508 (1987)

72. W. Koechner, Thermal lensing in a Nd:YAG laser rod, *Appl. Opt.* 9 (11), 2548 (1970)

73. M. E. Innocenzi *et al.*, Thermal modeling of continuous-wave end-pumped solid-state lasers, *Appl. Phys. Lett.* 56, 1831 (1990)

74. S. De Silvestri *et al.*, Rod thermal lensing effects in solid-state laser ring resonators, *Opt. Commun.* 65 (5), 373 (1988)

75. L. Yan and C. H. Lee, Thermal effects in end-pumped Nd:phosphate glasses, *J. Appl. Phys.* 75 (3), 1286 (1994)

76. J. L. Blows *et al.*, Heat generation in Nd:YVO4 with and without laser action, *IEEE Photon. Technol.* Lett. 10 (12), 1727 (1998)

77. P. J. Hardman *et al.*, Energy-transfer upconversion and thermal lensing in high-power end-pumped Nd:YLF laser crystals, *IEEE J. Quantum Electron.* 35 (4), 647 (1999)

78. A. Soloviev *et al.*, Experimental study of thermal lens features in laser ceramics, *Opt. Express* 16 (25), 21012 (2008)

79. P. A. Loiko *et al.*, Thermo-optic coefficients and thermal lensing in Nd-doped KGd(WO4)2 laser crystals, *Appl. Opt.* 49 (34), 6651 (2010)

80. R. L. Aggarwal *et al.*, Measurement of thermo-optic properties of Y3Al5O12, Lu3Al5O12, YAlO3, LiYF4, LiLuF4, BaY2F8, KGd(WO4)2, and KY(WO4)2 laser crystals in the 80–300 K temperature range, *J. Appl. Phys.* 98 (10), 103514 (2005)

81. N. Hodgson *et al.*, High power TEM00 mode operation of diode-pumped solid-state lasers, *Proc. SPIE* 3611, 119 (1999)

82. K. R. Hansen *et al.*, Thermo-optical effects in high-power ytterbium-doped fiber amplifiers, *Opt. Express* 19 (24), 23965 (2011)

83. G. Wagner *et al.*, Simulations of thermal lensing of a Ti:sapphire crystal end-pumped with high average power, *Opt. Express* 13 (20), 8045 (2005)

84. P. F. Moulton, Spectroscopic and laser characteristics of Ti:Al2O3, *J. Opt. Soc. Am. B* 3 (1), 125 (1986)

85. Yehoshua Y. Kalisky, *The Physics and Engineering of Solid State Lasers*, (*SPIE Press* 2006)

86. E. Gulevich *et al.*, Current state and prospects for tunable titanium–sapphire lasers, *Proc. SPIE* 2095, 102 (1994)

87. K. F. Wall, R. L. Aggarwal, M. D. Sciacca, H. J. Zeiger, R. E. Fahey, and A. J. Strauss, Optically induced nonresonant changes in the refractive index of Ti:Al2O3, *Opt. Lett.* 14(3), 180–182 (1989)

88. H. Eilers, E. Strauss, and W. M. Yen, Photoelastic effect in Ti3 -doped sapphire, *Physical Review B* 45 (17), 9604–9610 (1992)

89. T. A. Planchon, W. Amir, C. Childress, J. A. Squier, and C. G. Durfee, Measurement of pump-induced transient lensing in a cryogenically-cooled high average power Ti:sapphire amplifier, *Opt. Express* 16 (23), 18557–18564 (2008)

90. H. Raether, *Surface Plasmons*, (Springler-Verlag, Berlin, 1988)

91. H. Raether, *Excitation of Plasmons and Interband Transitions by Electrons*, Springer Tracts in Modern Physics, Vol. 88 (Springer, Berlin, Heidelberg, New York 1980)

92. V. K. Valev, *Investigation of Ferromagnetic/Antiferromagnetic Interfaces with Magnetization-Induced Second Harmonic Generation* (ISBN-10:90-9021353-8; 2006)

93. H. B. Zhao, *Optical Characterization of Ferromagnetic Heterostructure Interfaces and Thin Films* (A dissertation presented to faculty of Department of Applied Science, the College of William and Mary, 2006)

94. B. Koopmans, M. G. Koerkamp, and Th. Rasing, Observation of large Kerr angles in the nonlinear optical response from magnetic multilayers. *Phys. Rev. Lett.* 74, 3692-3695 (1995)

95. G. Spierings, V. Koutsos,V., H. A. Wierenga, Th. Rasing., *et al.* Interface magnetism studied by optical second harmonic generation. *Journal of Magnetism and Magnetic Materials.* 121,109-111 (1993)

96. I. Razdolski, D. G. Gheorghe, E. Melander, Th. Rasing, *et al.* Nonlocal nonlinear magneto-optical response of a magnetoplasmonic crystal. *Phys.Rev.B* 88, 075436 (2013)

97. C. Daboo, R. J. Hicken, D. E. P. Eley, *et al.* Magnetization reversal processes in epitaxial Fe/GaAs(001) films. *App.Phys.Lett.* 75,5586 (1994)

98. R. P. Cowburn, S. J. Gray, J. Ferre, *et al.* Magnetic switching and in-plane uniaxial anisotropy in ultrathin Ag/Fe/Ag(100) epitaxial films. *App.Phys.Lett.* 78,7210 (1995)

99. C. Daboo, R. J. Hicken, E. Gu, *et al.* Anisotropy and orientational dependence of magnetization reversal processes in epitaxial ferromagnetic thin films. *Phys.Rev.B* 51,15964 (1999)

100. http://www.rp-photonics.com/kerr_lens.html

101. http://www.rp-photonics.com/thermal_lensing.html

102. V. Ramanathan, J. Lee, S. Xu, X. Wang, and D. H. Reitze, Analysis of thermal aberrations in a high average power single-stage Ti:sapphire regenerative chirped pulse amplifier: simulation and experiment, *Rev. Sci. Instrum.* 77, 103103 (2006)

103. R. Weber, B. Neuenschwander, M. Mac Donald, M. B. Roos, and Heinz P.Weber, Cooling schemes for longitudinally diode laser-pumped Nd:YAG rods, *IEEE J. Quantum Electron.* 34 (1998)

104. M. Gottlieb, CRC Handbok of Laser Sciences and Technology, edited by M. J. Weber (CRC) Vol. IV, p. 319. (1986)

105. Harold Earl Bennett, Laser-induced Damage in Optical Materials, 1990: Proceedings, 22nd Annual Boulder Damage Symposium, 24-26 October 1990, Boulder, Colorado, Volume 1441

106. http://en.wikipedia.org/wiki/Sapphire

107. K. F. Wall and A. Sanchez, Titanium Sapphire Lasers, *THE LINCOLN LABORATORV JOURNAL VOLUME* 3. NUMBER 3 (1990)

108. P. F. Moulron, Ti-doped Sapphire Tunable Solid State Laser, *Opt. News* 8,9 (Nov./Dec. 1982)

109. P. F. Moulron, Specrroscopic and Laser Characrerisrics of Ti:Alz03. *Opt. Soc. Am. B3,* 125 (1986)

110. J. F. Nye, *Physical Properties of Crystals* (Clarendon, 1957)

111. T. S. Narasirnhamurty, Photoelastic and Electro-Optic Properties of Crystals (Plenum, New York, 1981)

112. R. Gould, R Gordon, The LASER, Light Amplification by Stimulated Emission of Radiation. In Franken, P.A. and Sands, R.H. (Eds.). *The Ann Arbor Conference on Optical Pumping, the University of Michigan, 15 June through 18 June 1959.* p. 128.

113. http://en.wikipedia.org/wiki/Mode-locking

114. http://www.rp-photonics.com/chirped_pulse_amplification.html

115. http://en.wikipedia.org/wiki/Kerr-lens_mode-locking

116. http://en.wikipedia.org/wiki/Amplified_spontaneous_emission

117. S. Y. Zhang, "Spatial Beam Shaping of High Power Ultra Short Laser Pulses" (A dissertation presented to faculty of Department of Applied Science, the College of William and Mary, 2007)

118. E. Martin, *et al.*, Ultrafast Lasers: Technology and Applications, (CRC Press, 2002)

119. H. E. Bennett, L. L. Chase, A. H. Guenther, *et al.* Laser-Induced Damage In Optical Materials: 1993, Proceedings, 25th Annual Boulder Damage Symposium.

120. http://www.newport.com/store/genContent.aspx/Laser-Damage-Threshold/144932/1033

121. A. E. Siegman, Ray optics and ray matrices, in Lasers, A. Kelly, ed. (University Science Books, 1986).

122. http://www.photonics.com/Article.aspx?AID=39225

123. J. Pistora, M. Lesnak, O. Vlasin, *et al.* Surface plasmon resonance sensor with Magneto-Optical thin film. *Acta Electrotechnica et Informatica,* Vol. 10, No. 3, 19–21 (2010)

124. D. M. Newman, M. L. Wears, R. J. Matelon, and D. Mchugh, Non-linear optics and magneto-optics on nano-structured interfaces, *Appl. Phys. B* **74**, 719–722 (2002)

125. V. K. Valev, A. V. Silhanek, W. Gillijns, Y. Jeyaram, H. Paddubrouskaya, A. Volodin, C. G. Biris, N. C. Panoiu, B. De Clercq, M. Ameloot, O. A. Aktsipetrov, V. V. Moshchalkov, and T. Verbiest, Plasmons reveal the direction of magnetization in nickel nanostructures, *ACS Nano* **5**, 91–96 (2011)

126. P. Berini, Long-range surface plasmon polaritons, *Advances in Optics and Photonics* **1**, 484–588 (2009)

127. G. J. Kovacs, Surface polariton in the ATR angular spectra of a thin iron film bounded by dielectric layers, *J. Opt. Soc. Am.* **68**, 1325–1332 (1978)

128. K. Aslan, M. Weisenberg, E. Hortle, and C. D. Geddes, Surface plasmon coupled chemiluminescence from iron thin films: directional and approaching fixed angle observation, *J. Appl. Phys.* **106,** 014131 (2009)

129. M. A. Ordal, L. L. Long, R. J. Bell, S. E. Bell, R. R. Bell, R. W. Alexander, Jr., and C. A. Ward, Optical properties of the metals Al, Co, Cu, Au, Fe, Pb, Ni, Pd, Pt, Ag, Ti, and W in the infrared and far infrared, *Appl. Opt.* **22**(7), 1099-1120 (1983)